Research Square

Preprints are preliminary reports that have not undergone peer review.
They should not be considered conclusive, used to inform clinical practice,
or referenced by the media as validated information.

Actuation-dependent plume geometry in nasal spray delivery of lipid nanoparticles influences nasal deposition site and particle integrity

Ji-Seung Kim
Chungbuk National University
Jin-Hyuk Jeong
Chungbuk National University
Yu-Rim Choi
Chungbuk National University
Woong-Young Jung
Chungbuk National University
Ji-Hyeon Kwon
Chungbuk National University
Yuseon Shin
Chungbuk National University
Hye Jin Lee
Chungbuk National University
Dae Hwan Shin
Chungbuk National University
Chun-Woong Park
cwpark@chungbuk.ac.kr

Chungbuk National University

Research Article

Keywords: Nasal spray, Actuation parameters, Plume geometry, Nasal deposition, Lipid nanoparticles, mRNA delivery

Posted Date: September 28th, 2026

DOI: https://doi.org/10.21203/rs.3.rs-11037329/v1

License: This work is licensed under a Creative Commons Attribution 4.0 International License.
Read Full License

Additional Declarations: No competing interests reported.

Actuation-dependent plume geometry in nasal spray delivery of lipid nanoparticles influences nasal deposition site and particle integrity

Ji-Seung Kim[1]†, Jin-Hyuk Jeong[1]†, Yu-Rim Choi[1], Woong-Young Jung[1], Ji-Hyeon Kwon[1], Yuseon Shin[1], Hye Jin Lee[1], Dae Hwan Shin[1], Chun-Woong Park[1*]

[1]College of Pharmacy, Chungbuk National University, Cheongju 28160, Republic of Korea; ktg295277@daum.net (JSK), jinddong92@gmail.com (JHJ), 2023ddtr@naver.com (YRC) woongyj913@naver.com (WYJ), wnltns2@chungbuk.ac.kr (JHK), shiny@chungbuk.ac.kr (YSS), hyejinlee@chungbuk.ac.kr (HJL), dshin@chungbuk.ac.kr (DHS)

† Ji-Seung Kim and Jin-Hyuk Jeong contributed equally to this work.

***Corresponding authors**

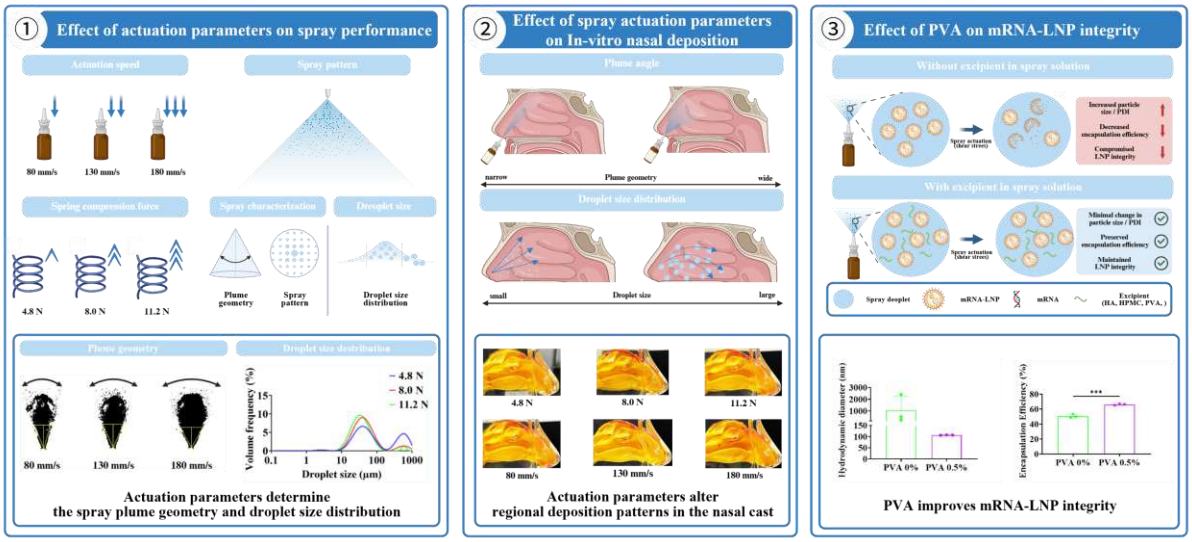
Chun-Woong Park

College of Pharmacy, Chungbuk National University, Cheongju 28160, Republic of Korea

Tel.: +82-43-261-3330

Email: cwpark@chungbuk.ac.kr

Graphical Abstract



s

Abstract

Intranasal administration provides a non-invasive approach to the nose-to-brain delivery of messenger RNA (mRNA) therapeutics; however, effective delivery requires both targeted deposition in the superior nasal region and preservation of lipid nanoparticle (LNP) integrity during spray actuation. Although the performance of mechanical nasal spray pumps depends strongly on their mode of actuation, the effects of actuation conditions on regional nasal deposition and mRNA-LNP stability have rarely been evaluated concurrently. Here, a mechanical nasal spray device was evaluated at three spring compression forces (4.8, 8.0, and 11.2 N) and actuation speeds of 80–180 mm/s. Plume geometry, spray pattern, droplet size distribution, and single-actuation content and volume were characterized, followed by regional deposition analysis in a three-dimensional nasal cast. A higher compression force significantly enhanced deposition in the superior turbinate region, whereas increasing the actuation speed shifted deposition toward the middle turbinate. Following actuation of the mRNA-LNPs, encapsulation efficiency significantly decreased under all conditions and was a more sensitive indicator of instability than particle size, indicating that device actuation alone did not preserve LNP integrity. Incorporating viscosity-enhancing excipients suppressed actuation-induced aggregation. Among these excipients, poly(vinyl alcohol) (PVA) was selected for further characterization. The addition of 0.5% PVA increased droplet size without altering plume geometry and significantly increased middle-turbinate deposition. Collectively, these findings demonstrate that nasal spray actuation and formulation both govern regional nasal targeting and mRNA-LNP stability, underscoring the need to co-optimize device performance and formulation when developing nasal spray systems for the nose-to-brain delivery of mRNA-LNPs.

Keywords

Nasal spray; Actuation parameters; Plume geometry; Nasal deposition; Lipid nanoparticles; mRNA delivery

Introduction

As the global population ages, central nervous system (CNS) disorders, such as Alzheimer's disease, Parkinson's disease, and migraine have become major health and societal burdens and remain among the therapeutic areas with the greatest unmet clinical need [1, 2]. A principal obstacle to treating CNS diseases is the blood–brain barrier (BBB), which prevents more than 98% of small-molecule drugs and nearly all macromolecular therapeutics from entering the brain parenchyma [3, 4]. Consequently, many pharmacologically active agents fail to reach therapeutic concentrations in the CNS despite demonstrating promising preclinical activity [5]. Accordingly, a range of nanocarrier-based strategies has been explored to improve drug delivery to the brain in neurodegenerative and neuro-oncological conditions [6].

Among emerging therapeutic modalities, messenger RNA (mRNA) has rapidly evolved from a vaccine platform into a versatile technology with applications in protein-replacement therapy, gene editing, and cancer immunotherapy [7, 8]. Its clinical translation has been enabled by lipid nanoparticles (LNPs), which protect the labile mRNA cargo, mediate intracellular delivery, and support scalable manufacturing [9, 10]. The therapeutic performance of these nanoparticle systems depends closely on their physicochemical attributes, including particle size, encapsulation efficiency, and colloidal stability, which must be preserved from preparation through administration [11]. As the applications of mRNA therapeutics expand to include chronic diseases and CNS disorders, the route of administration has become a critical determinant of therapeutic efficacy and patient accessibility [12].

Among non-invasive routes, intranasal administration is particularly attractive for delivering LNP-based therapeutics to the CNS [13]. The nasal cavity provides direct anatomical connections to the brain through the olfactory and trigeminal nerve pathways, allowing a fraction of the administered dose to reach the brain while bypassing first-pass metabolism and the BBB [14]. This nose-to-brain (N2B) route has generated growing interest in nasal sprays as a practical dosage form for CNS-targeted nanomedicines, and several nasal spray products have already been clinically approved for CNS indications [15, 16]. However, the efficiency of N2B delivery is constrained by the complex geometry of the nasal airway. A large fraction of an intranasally administered dose is deposited prematurely in the anterior and respiratory regions and subsequently cleared through mucociliary action rather than reaching the superior turbinate region deep within the nasal cavity, which is associated with olfactory transport to the brain [17, 18].

The regional deposition of a nasal spray is governed largely by the performance of the delivery device. Aqueous spray pumps, which dominate the nasal drug-delivery market, rely on actuation force to atomize the formulation.

The resulting spray characteristics—including plume geometry, spray pattern, and droplet size distribution—collectively determine regional dose deposition within the nasal cavity [19, 20]. Because these pumps are spring-driven and metered, their spray characteristics depend strongly on how the device is actuated. Parameters such as spring compression force, actuation speed, and actuation acceleration govern the pressure at which the formulation is atomized and, consequently, the size and momentum of the emitted droplets [21, 22]. Comparable device- and process-level parameters are known to govern aerosol performance across inhalation platforms more broadly [23]. However, the relationship between these actuation parameters and regional deposition within the nasal cavity remains incompletely defined, particularly with respect to the effect of spring compression force on deposition in the superior nasal region relevant to N2B delivery[24].

In addition to determining deposition, the actuation process exposes the formulation to mechanical and interfacial stresses that may compromise the integrity of the nanoparticle cargo. During atomization, LNPs are subjected to shear forces and repeated formation of air–liquid interfaces. These stresses have been shown to cause particle aggregation, increased particle size and polydispersity, and loss of mRNA encapsulation [25, 26]. These effects, which are well documented for nebulization and inhalation, can substantially reduce the deliverable payload before it reaches its target [27, 28]. Consistent with these observations, aerosolization and related processing have been reported to alter the physical characteristics of inhalable lipid-based particles [29]. Effective nasal delivery of mRNA-LNPs therefore requires both favorable regional deposition and preservation of nanoparticle integrity throughout the spray process. However, these requirements have rarely been evaluated together within a single delivery system [30].

The formulation itself can further influence nasal spray behavior, and the inclusion of stabilizing excipients represents one strategy for mitigating atomization-induced damage. Surface-active and viscosity-modifying polymers, such as poly(vinyl alcohol) (PVA), cellulose derivatives, and hyaluronic acid, are widely used to stabilize nanoparticle and colloidal systems by adsorbing onto particle surfaces and modulating interfacial behavior [31–33]. Hyaluronic acid–based carriers, in particular, have been engineered as self-assembling and surface-functionalized nanosystems with tunable colloidal behavior [34]. Such excipients may therefore help preserve nanoparticle integrity under the interfacial and shear stresses generated during actuation. Notably, viscosity-modifying excipients have also been reported to improve the regional targeting of nasal sprays toward the superior nasal cavity, thereby linking formulation composition to both deposition and stability [35, 36].

In the present study, we investigated two consequences of nasal spray actuation that are typically examined

separately: how actuation conditions influence spray performance and, consequently, regional nasal deposition, and how the same actuation process affects mRNA-LNP integrity. Using an automated actuator to provide reproducible, operator-independent control of a mechanical, spring-driven nasal spray pump, we varied the spring compression force and actuation speed and characterized their effects on plume geometry, spray pattern, droplet size distribution, and single-actuation content and volume. Regional deposition was subsequently mapped in a three-dimensional nasal cast, and the physicochemical integrity of mRNA-loaded LNPs was assessed before and after actuation under each condition. Finally, stabilizing excipients were screened for their ability to preserve LNP integrity during actuation. Based on this screening, PVA was selected for further characterization to determine whether a viscosity-modifying excipient could modulate spray performance and regional nasal deposition, thereby complementing the device-driven effects. Together, these experiments demonstrate that actuation conditions and formulation jointly shape regional nasal deposition and nanoparticle stability, underscoring the need to co-optimize device performance and formulation robustness when developing nasal spray systems for mRNA delivery.

Materials and Methods

Materials

The ionizable lipid ALC-0315, polyethylene glycol (PEG)-lipid ALC-0159, and phospholipid 1,2-distearoyl-*sn*-glycero-3-phosphocholine (DSPC; 18:0 PC) were purchased from Avanti Polar Lipids (Merck KGaA, Darmstadt, Germany). Cholesterol was obtained from Sigma-Aldrich (Merck KGaA, Darmstadt, Germany). N1-methylpseudouridine-modified mRNA encoding mCherry (1 μg/μL) was obtained from VectorBuilder (Chicago, IL, USA). Anhydrous ethyl alcohol (99%, high-performance liquid chromatography [HPLC] grade), anhydrous citric acid, and sodium hydroxide (beads, 98%, extra pure) were purchased from Samchun Pure Chemical (Seoul, Korea). A 25 mM citrate buffer (pH 4.0) was prepared by dissolving citric acid in UltraPure water and adjusting the pH to 4.0 with sodium hydroxide for use in LNP formulation. UltraPure DNase/RNase-free distilled water was obtained from Invitrogen (Thermo Fisher Scientific, Grand Island, NY, USA). The Quant-iT RiboGreen RNA Assay Kit (R11490) and Triton X-100 used for analysis were obtained from Invitrogen (Thermo Fisher Scientific, Eugene, OR, USA) and Merck KGaA (Darmstadt, Germany), respectively. Water-finding paste (Kolor Kut; Kolor Kut Products, Houston, TX, USA) was used in the nasal cast deposition study.

For excipient screening, sodium hyaluronate (Hyatrue HA-EP1; Bloomage Biotechnology, Jinan, China), hydroxypropyl methylcellulose (HPMC; Metolose 90SH-4000SR; Shin-Etsu Chemical, Tokyo, Japan), and polyvinyl alcohol 2000 (PVA 2000; Samchun Pure Chemical, Seoul, Korea) were used as stabilizing excipients. All other reagents were of analytical grade.

Nasal spray device and actuation

Formulations were dispensed using a VP7 pre-compression nasal spray pump (Aptar Pharma, Le Vaudreuil, France). To ensure reproducible, operator-independent actuation, spraying was controlled using a Vereo automated actuator (NSx) operated with Viota software (Proveris Scientific, Marlborough, MA, USA). Three springs with compression forces of 4.8, 8.0, and 11.2 N were evaluated. Five actuation profiles were programmed. Methods 1–3 used actuation speeds of 80, 130, and 180 mm/s, respectively, at a fixed acceleration of 4,000 mm/s². Methods 3–5 used accelerations of 4,000, 8,000, and 12,000 mm/s², respectively, at a fixed actuation speed of 180 mm/s. The hold time was fixed at 160 ms for all profiles.

Plume geometry and spray characterization

Plume geometry and spray characteristics were characterized by high-speed imaging according to the principles described in the US Food and Drug Administration (FDA) guidance for nasal spray products [37]. The spray was actuated vertically upward through a horizontally positioned laser sheet, and side-view images were recorded at 8,000 frames per second using a high-speed camera (HAS-D71; Ditect, Tokyo, Japan) with a resolution of 640 × 480 pixels and a shutter speed of 1/8,000 s.

The plume angle was defined as the cone angle originating from a vertex at the actuator orifice, whereas plume height was defined as the distance along the spray axis from the orifice to the leading edge of the plume. Both parameters were determined from individual snapshot images. The projected spray area was determined from time-averaged images acquired at distances of 3 and 6 cm from the actuator orifice. All image sequences were

processed using Flownizer64 (version 1.2.12; Ditect, Tokyo, Japan), and representative images were prepared using Adobe Photoshop 2024 (Adobe, San Jose, CA, USA).

Droplet size distribution

Droplet size distribution was measured by laser diffraction using a Spraytec system (Malvern Panalytical, Malvern, UK) at distances of 3 and 6 cm from the actuator orifice, in accordance with the FDA guidance for nasal spray products [37];The measurement positions were separated by 3 cm and were within the recommended measurement range. The spray was directed through the laser beam, and the optical model was configured with a particle refractive index of 1.33 for water in air, with multiple-scattering analysis enabled. Droplet size was reported on a volume basis over a measurement range of 0.1–2,500 μm.

Because the actuation conditions varied widely, a consistent, fully developed plume phase could not be defined across all conditions. Data were therefore extracted using a fixed transmission-based criterion. Specifically, droplet size parameters were determined over the period during which light transmission remained below 90%, representing the actively developed phase of the spray. The volume median diameter (Dv50) and Sauter mean diameter (D[3,2]) were determined over this period. The proportion of the measurement period during which transmission remained below 90% was additionally recorded as an index of spray development.

Single-actuation mRNA content and volume

The single-actuation volume was determined gravimetrically by weighing the device before and after each actuation and converting the difference in mass to volume using the formulation density [37, 38]. To determine the single-actuation content, the spray emitted during one actuation was collected in a microcentrifuge tube and diluted with UltraPure DNase/RNase-free distilled water. The amount of mRNA delivered per actuation was then quantified using the Quant-iT RiboGreen RNA assay according to the manufacturer's instructions. The mRNA concentration was determined using a standard curve prepared with the ribosomal RNA standard supplied with the kit. The relationship between single-actuation mRNA content and volume was evaluated across all spring

compression forces and actuation speeds. The theoretical content–volume relationship was calculated based on the mRNA concentration of the LNP formulation.

Regional deposition in the nasal cast

Regional deposition was evaluated using a silicone nasal cast divided into five anatomical regions: nasal vestibule, inferior turbinate, middle turbinate, superior turbinate, and nasopharynx. Before actuation, water-finding paste (Kolor Kut) was applied to the internal surfaces of the cast. Upon contact with the deposited aqueous spray, the paste changed from its original color to red, enabling the regions of deposition to be identified.

Deposition was evaluated as a function of spring compression force at a fixed actuation speed of 80 mm/s (Method 1) and as a function of actuation speed using the 11.2 N spring. After actuation, the cast was imaged, and the areas exhibiting red color development were quantified using Fiji (ImageJ). Deposition in each anatomical region was calculated as the ratio of the red-stained area within each region to the total red-stained area, expressed as a percentage.

LNP preparation

mRNA-loaded LNPs were prepared by flash nanoprecipitation using a NanoFabTx NanoFlash confined impinging jet (CIJ) device (Sigma-Aldrich, Merck KGaA, Darmstadt, Germany). The lipid phase consisted of ALC-0315, DSPC, cholesterol, and ALC-0159 at a molar ratio of 47.5:10:40.5:2, based on the lipid composition of a clinically approved mRNA vaccine [39], and was dissolved in anhydrous ethanol. The aqueous phase consisted of mCherry-encoding mRNA in 25 mM citrate buffer (pH 4.0). The two phases were combined at a nitrogen-to-phosphate (N/P) ratio of 20. Using syringe pumps, the aqueous and lipid phases were mixed by impingement in the CIJ device at a flow rate ratio (aqueous:ethanol) of 5:1 and a total flow rate of 12 mL/min. The resulting LNP dispersion was diluted 1:1 (v/v) with phosphate-buffered saline (PBS) and stored at 4 °C until use.

Physicochemical characterization of LNPs

The hydrodynamic diameter, polydispersity index (PDI), and zeta potential of the LNPs were measured by dynamic light scattering using a Litesizer 500 (Anton Paar, Graz, Austria) [40]. Before measurement, the samples were diluted in UltraPure DNase/RNase-free distilled water. Measurements were performed at 25 °C after a 5-min equilibration period, using an automatically selected measurement angle and three runs per sample. Particle size was analyzed using the cumulant method in accordance with ISO 22412.

Encapsulation efficiency (EE) was determined using the Quant-iT RiboGreen RNA assay by quantifying free (unencapsulated) mRNA in the absence of detergent and total mRNA in the presence of 0.5% Triton X-100. EE was calculated using the following equation:

$$EE\ (\%) = \frac{total\ mRNA - free\ mRNA}{total\ mRNA} \times 100$$ [41].

All physicochemical parameters were measured before (pre-actuation) and after actuation.

Excipient screening for LNP stabilization

Three excipients—sodium hyaluronate, HPMC, and PVA 2000 [31]—were evaluated for their ability to stabilize the LNPs against actuation-induced stress. Each excipient was dissolved in PBS at 1% (w/v) and mixed with the LNP dispersion at a 1:1 (v/v) ratio, resulting in a final excipient concentration of 0.5% (w/v). Immediately after mixing, the excipient-containing LNP formulations were actuated using a spring compression force of 11.2 N and an actuation speed of 80 mm/s (Method 1). Hydrodynamic diameter, PDI, encapsulation efficiency, and zeta potential were measured before and after actuation.**Statistical analysis**

All data are presented as the mean ± standard deviation (SD) (n = 3). Statistical comparisons were performed using one-way analysis of variance (ANOVA), followed by Tukey's post hoc test using GraphPad Prism version 8.4.2 (GraphPad Software, San Diego, CA, USA). Differences were considered statistically significant at $p < 0.05$.

Use of generative AI

During the preparation of this work, the authors used an AI-assisted tool (Claude, Anthropic, San Francisco, CA, USA) to assist with language editing, drafting, and improving the clarity of the manuscript. After using this tool, the authors reviewed and edited all content as required and take full responsibility for the content of the published article.

Results

Physicochemical properties of the mRNA-loaded LNPs

The mRNA-loaded LNPs were first characterized for their physicochemical properties (**Fig. 1**). The hydrodynamic diameter was approximately 90 nm irrespective of mRNA loading, with no significant difference between blank (LNP (BLK)) and mRNA-loaded (LNP (RNA)) particles (**Fig. 1a)**. Both formulations exhibited comparably low polydispersity indices (**Fig. 1b**) and near-neutral surface charges, with no meaningful difference in zeta potential (**Fig. 1c**). Cryogenic transmission electron microscopy revealed spherical, well-dispersed particles with consistent sizes in both formulations, in agreement with the dynamic light scattering measurements (**Fig. 1d**).

The colloidal stability of the mRNA-loaded LNPs was subsequently evaluated during storage at 4 °C (**Fig. 1e–h**). During the first week of storage, the particle size remained approximately 100 nm (**Fig. 1e**), while the polydispersity index (**Fig. 1f**) and near-neutral zeta potential (**Fig. 1g**) remained essentially unchanged. The encapsulation efficiency was maintained above 90% over the same period (**Fig. 1h**), indicating that the mRNA-loaded LNPs retained their physical and colloidal stability under these storage conditions.

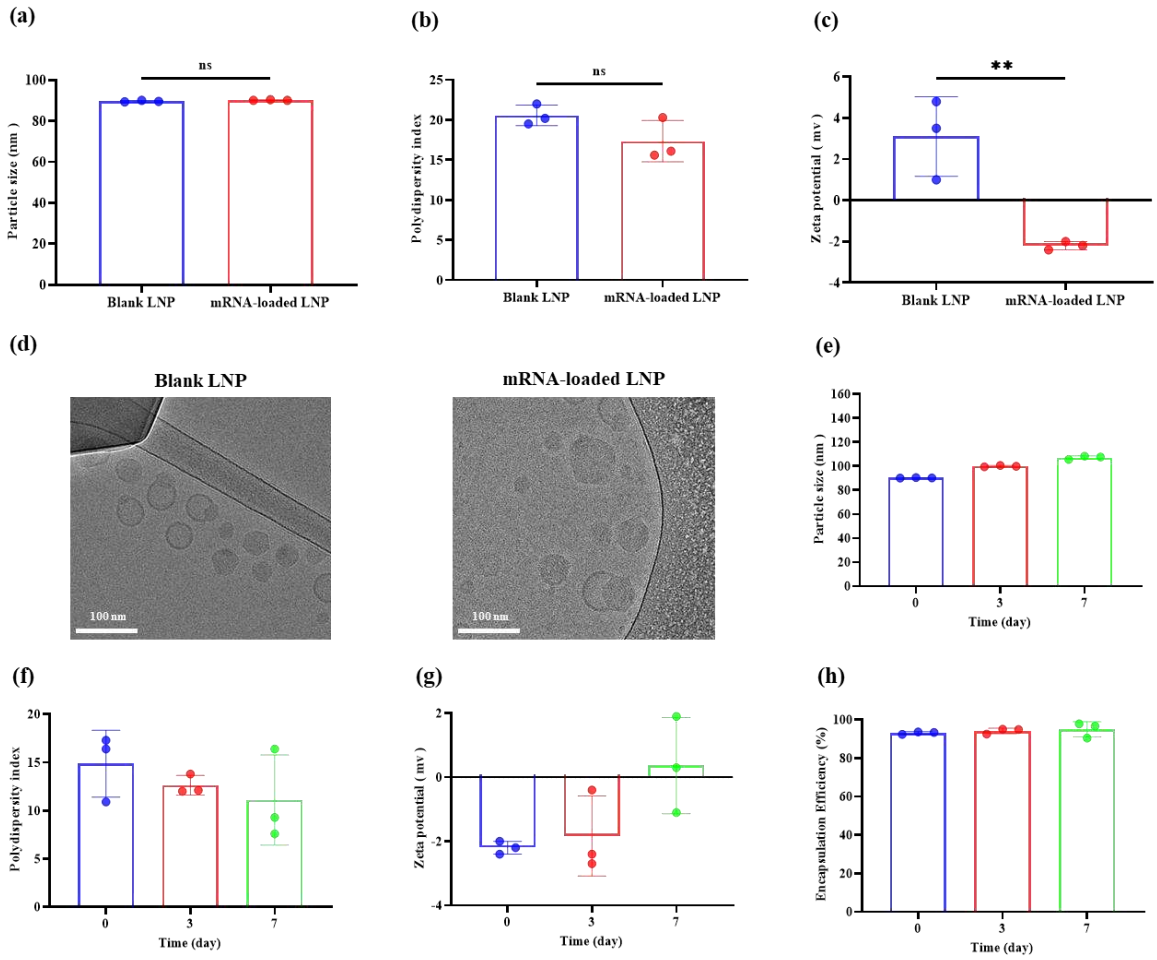


Fig. 1 Physicochemical characterization and colloidal stability of mRNA-loaded LNPs. **a–c** Particle size, polydispersity index, and zeta potential of blank LNPs (LNP (BLK)) and mRNA-loaded LNPs (LNP (RNA)). **d** Representative cryogenic transmission electron microscopy images of blank and mRNA-loaded LNPs. e–h Colloidal stability of mRNA-loaded LNPs during storage at 4 °C, as assessed by particle size, polydispersity index, zeta potential, and encapsulation efficiency over 14 days. Data are presented as the mean ± SD (n = 3); ns, not significant; **p < 0.01

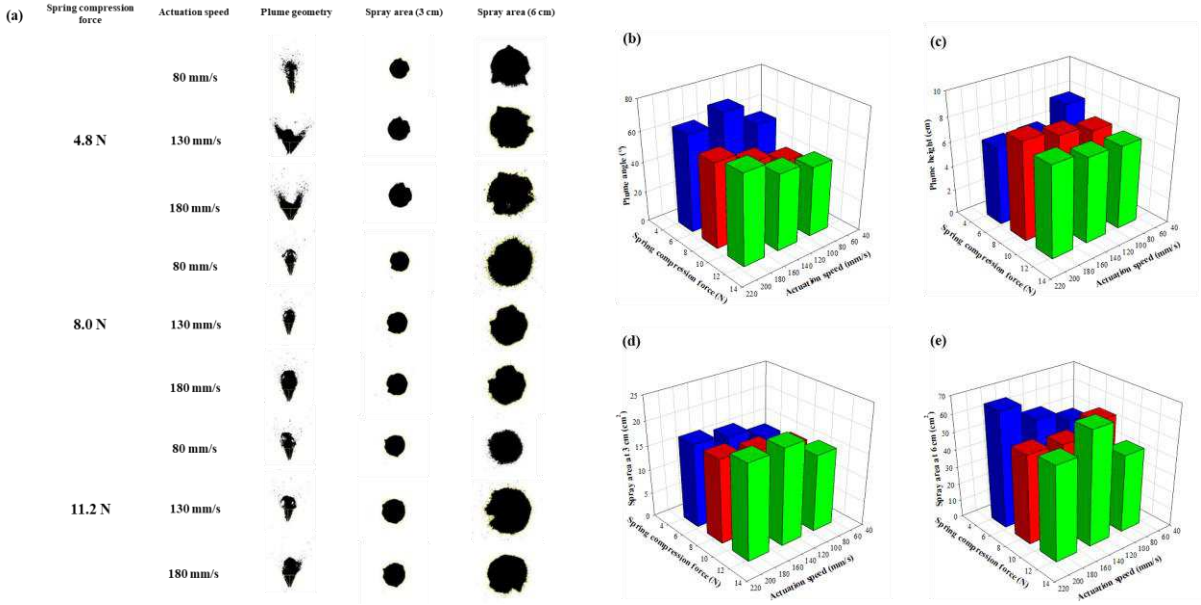
Plume geometry and spray pattern

The plume geometry and spray pattern varied with the actuation conditions, with the plume angle showing the most consistent dependence on actuation speed (**Fig. 2a, b**). For the stable sprays generated using the 8.0 and 11.2 N springs, the plume angle increased monotonically with actuation speed. For the 8.0 N spring, the angle increased from 40.2 ± 3.9° at 80 mm/s to 47.5 ± 6.2° at 130 mm/s and 55.9 ± 5.7° at 180 mm/s. Corresponding values for

the 11.2 N spring were 46.0 ± 4.1°, 50.2 ± 4.5° and 59.5 ± 6.2°, respectively. In contrast, the 4.8 N spring failed to generate a fully developed spray and instead produced a wide, unstable plume, with angles of 56.1 ± 10.3°, 70.6 ± 6.6°, and 64.0 ± 2.7° at 80, 130, and 180 mm/s, respectively. Consequently, no clear relationship between plume angle and actuation speed was observed for this spring. Plume height varied within a relatively narrow range of approximately 6–8 cm and showed a less systematic response to the actuation conditions (**Fig. 2c**). It increased modestly with actuation speed for the 8.0 and 11.2 N springs, whereas the 4.8 N spring exhibited a different pattern, producing its tallest plume at the lowest speed.

At 3 cm from the actuator orifice, the projected spray area generally increased with actuation speed and spring compression force, with the 11.2 N spring producing the largest areas: 15.85 ± 0.55, 19.79 ± 2.28, and 19.54 ± 1.60 cm^2 at 80, 130, and 180 mm/s, respectively (**Fig. 2d**). At 6 cm, the spray area was substantially larger under all conditions, ranging from approximately 45 to 70 cm^2, consistent with continued radial expansion of the plume with increasing distance. At this distance, however, the spray area was more variable across replicates and showed no consistent dependence on either actuation speed or compression force (**Fig. 2e**).

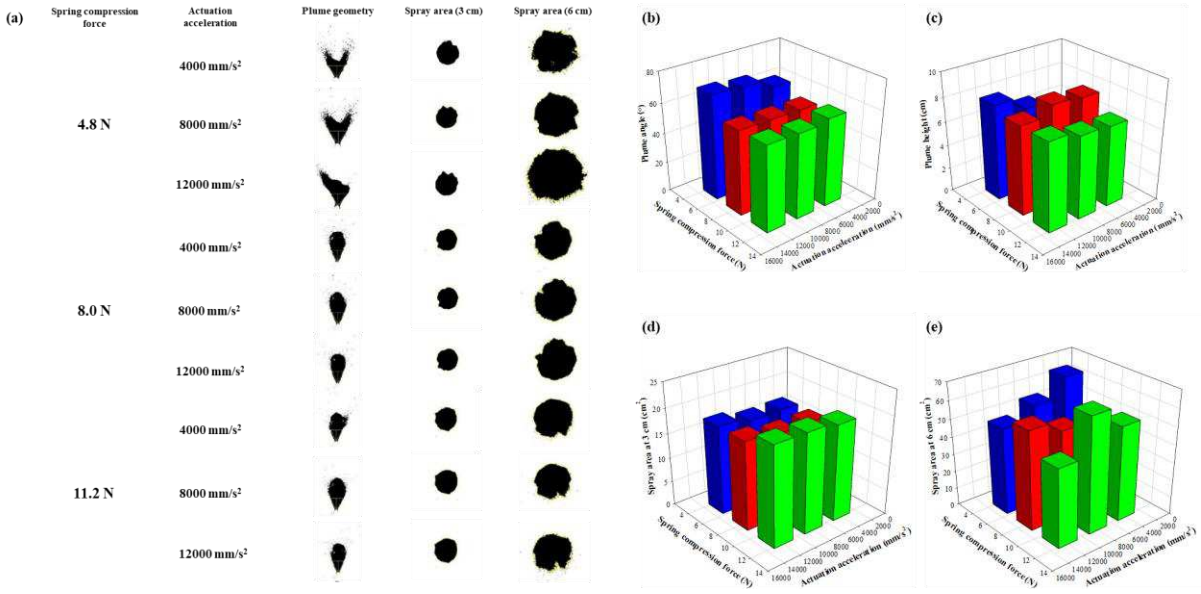
At a fixed actuation speed of 180 mm/s, varying the actuation acceleration from 4,000 to 12,000 mm/s^2 had only a minor effect on the plume geometry and spray pattern (**Fig. 3**). At each compression force, the plume angle (**Fig. 3b**), plume height (**Fig. 3c**), and projected spray areas at 3 and 6 cm (**Fig. 3d, e**) remained largely unchanged across the three acceleration levels. For example, with the 4.8 N spring, the plume angles were 64.0 ± 2.7°, 70.2 ± 2.7°, and 69.9 ± 3.1° at 4,000, 8,000, and 12,000 mm/s^2, respectively. The wide, unstable plume generated by the 4.8 N spring and the larger spray area at 3 cm produced by the 11.2 N spring, which reached 20.58 ± 1.83 cm^2, persisted across the tested acceleration levels. Nevertheless, actuation acceleration showed no consistent relationship with any of the measured parameters.



304

305 **Fig. 2** Plume geometry and spray pattern of the nasal spray as a function of spring compression force (4.8, 8.0,
306 and 11.2 N) and actuation speed (80, 130, and 180 mm/s) at a fixed actuation acceleration of 4,000 mm/s². **a**
307 Representative high-speed images of the plume (side view) and of the spray pattern at 3 and 6 cm from the actuator
308 orifice for each spring and actuation speed. **b** Plume angle. **c** Plume height. **d** Spray area at 3 cm. **e** Spray area at
309 6 cm. Bars represent the mean of three replicates (n = 3)

310



311

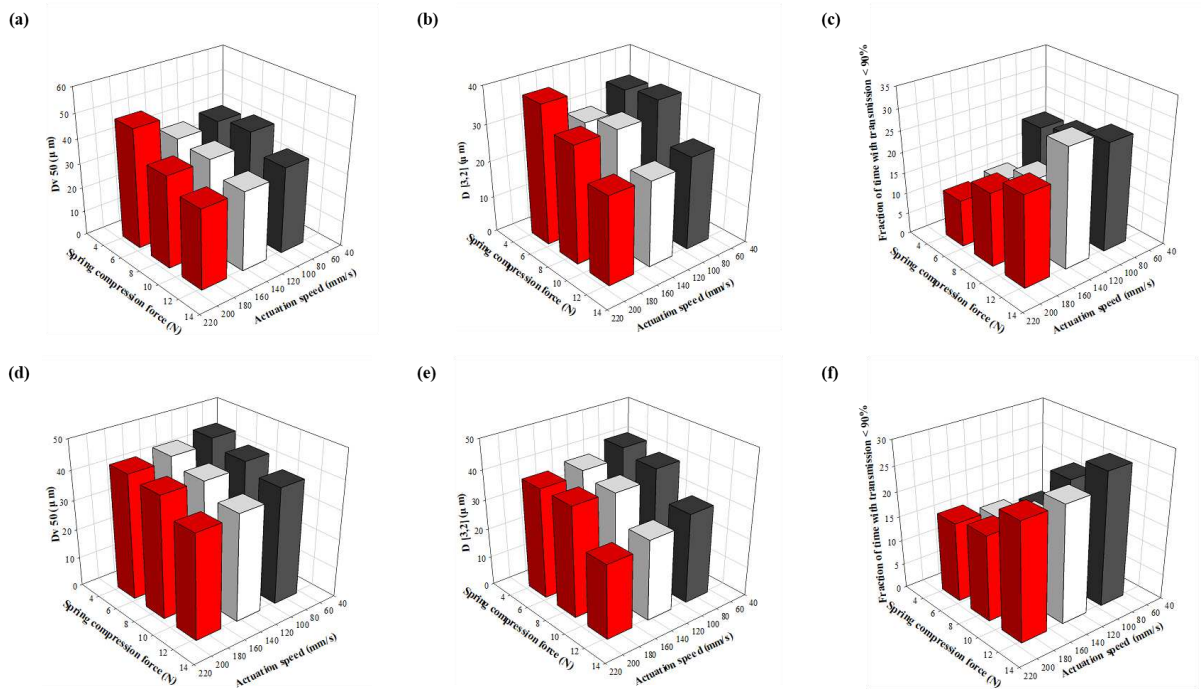
312 **Fig. 3** Effect of actuation acceleration on the plume geometry and spray pattern at a fixed actuation speed of 180
313 mm/s, evaluated at spring compression forces of 4.8, 8.0, and 11.2 N and actuation accelerations of 4,000, 8,000,

and 12,000 mm/s². **a** Representative high-speed images of the plume and of the spray pattern at 3 and 6 cm. **b** Plume angle. **c** Plume height. **d** Spray area at 3 cm. **e** Spray area at 6 cm. Bars represent the mean of three replicates (n = 3)

Droplet size distribution

The droplet size distribution was primarily dependent on the spring compression force (**Fig. 4**). Increasing the compression force produced finer droplets: the 11.2 N spring consistently yielded the smallest volume median diameter (Dv50) and Sauter mean diameter (D[3,2]), whereas the 4.8 N spring produced the coarsest and most variable droplets. At 180 mm/s and 3 cm, the Dv50 decreased from 48.6 µm at 4.8 N to 37.5 µm at 8.0 N and 32.6 µm at 11.2 N, with a corresponding decrease in D[3,2] (38.3, 32.1, and 24.0 µm, respectively); the same ordering was observed at 80 and 130 mm/s and at 6 cm. Conversely, the proportion of the measurement period during which light transmission was below 90% increased with compression force and was highest for the 11.2 N spring. At 180 mm/s and 3 cm, this proportion was 21.9% for the 11.2 N spring compared with 11.3% for the 4.8 N spring, consistent with the formation of a denser and more sustained spray. Although droplet sizes were slightly larger at 6 cm than at 3 cm, their dependence on compression force remained consistent.

At a fixed actuation speed of 180 mm/s, increasing the actuation acceleration from 4,000 to 12,000 mm/s² had only a limited effect on the droplet size distribution, while the dependence on spring compression force was maintained (**Fig. 5**). For the 8.0 and 11.2 N springs, the Dv50 remained essentially unchanged across the three acceleration levels. For example, with the 11.2 N spring at a measurement distance of 3 cm, the Dv50 values were 32.6, 32.1, and 32.1 µm at 4,000, 8,000, and 12,000 mm/s², respectively. The 4.8 N spring produced the coarsest and most variable droplets at all acceleration levels, with the Dv50 increasing further at the highest acceleration to 70.8 ± 17.6 µm at 3 cm. Consistent with the actuation-speed series, the proportion of the measurement period during which light transmission was below 90% increased with compression force.



338

339 **Fig. 4** Droplet size distribution of the nasal spray as a function of spring compression force (4.8, 8.0, and 11.2 N)
340 and actuation speed (80, 130, and 180 mm/s) at a fixed actuation acceleration of 4,000 mm/s², measured at 3 cm
341 (a–c) and 6 cm (d–f) from the actuator orifice. For each distance, the volume median diameter (Dv50; a and d),
342 Sauter mean diameter (D[3,2]; b and e), and proportion of the measurement period during which light transmission
343 was below 90% (c and f) are shown. Bars represent the mean of three replicates (n = 3)

344

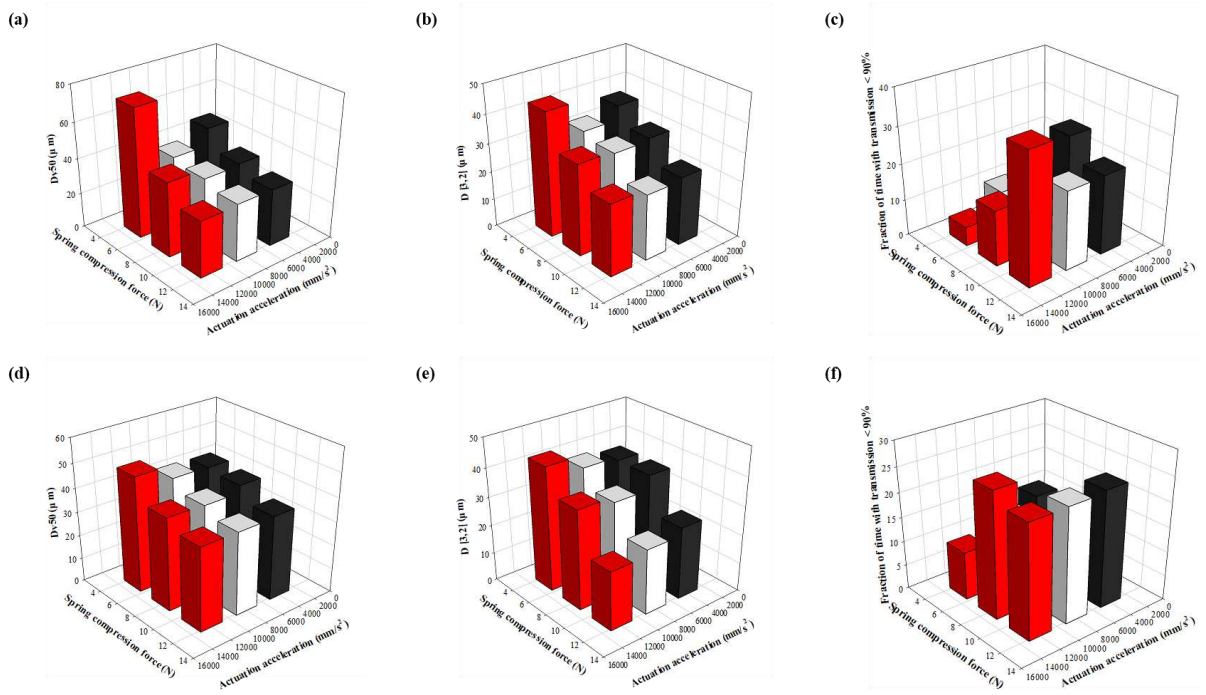


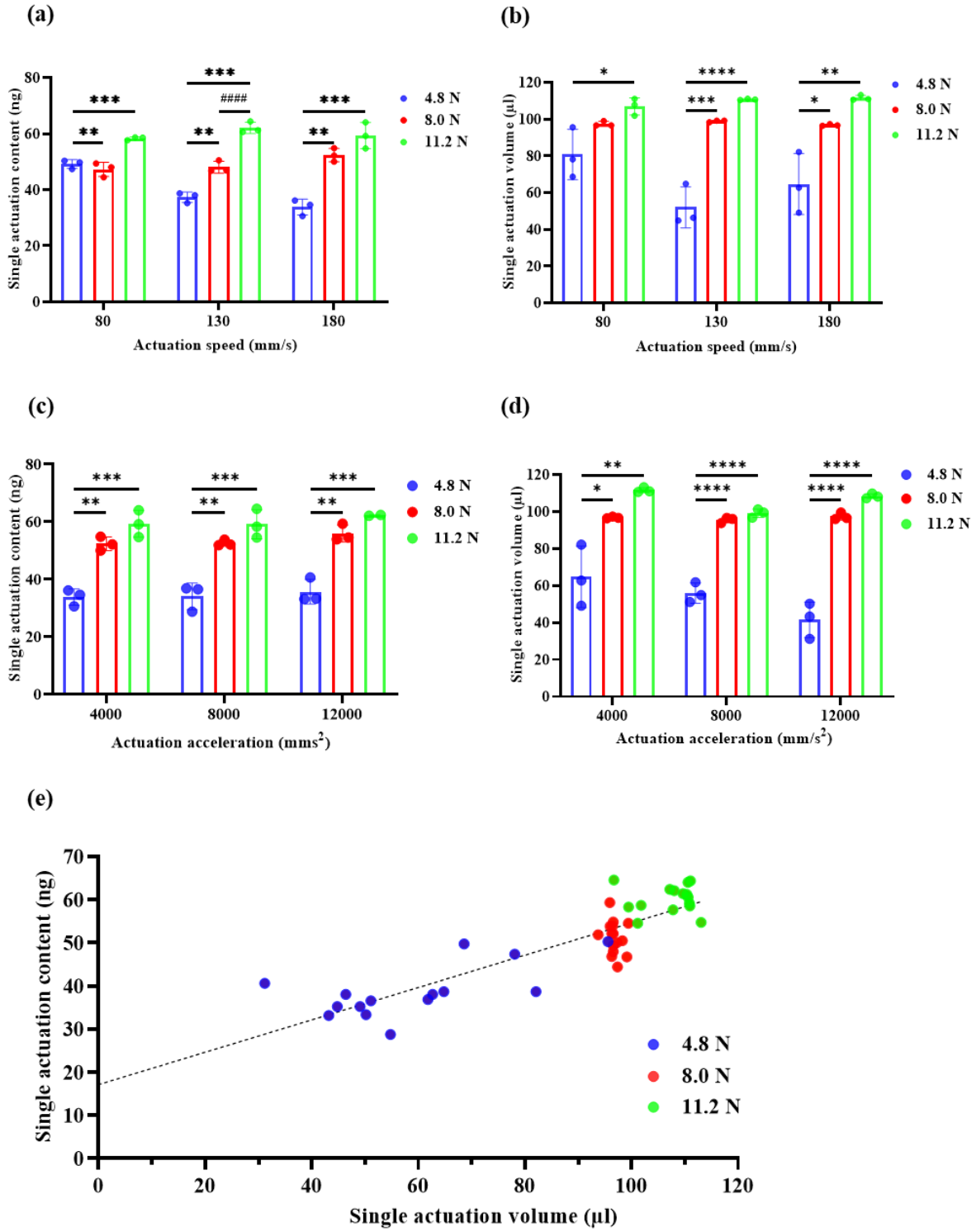
Fig. 5 Effect of actuation acceleration on the droplet size distribution at a fixed actuation speed of 180 mm/s. Measurements were obtained using spring compression forces of 4.8, 8.0, and 11.2 N and actuation accelerations of 4,000, 8,000, and 12,000 mm/s², measured at 3 cm (a–c) and 6 cm (d–f) from the actuator orifice. For each distance, the volume median diameter (Dv50; a and d), Sauter mean diameter (D[3,2]; b and e), and proportion of the measurement period during which light transmission was below 90% (c and f) are shown. Bars represent the mean of three replicates (n = 3)

Single-actuation mRNA content and volume

Both the single-actuation mRNA content and volume delivered per actuation increased with spring compression force under all actuation conditions (**Fig. 6a–d**). The 11.2 N spring consistently delivered the highest mRNA content and volume, whereas the 4.8 N spring delivered the lowest. The values obtained with the 8.0 and 11.2 N springs differed significantly from those obtained with the 4.8 N spring at every actuation speed and acceleration (**Fig. 6a–d**). In contrast, neither actuation speed nor actuation acceleration produced a consistent change in the delivered mRNA content or volume at a fixed compression force.

Plotting the delivered mRNA content against the emitted volume showed that both variables increased together along the theoretical constant-concentration line (**Fig. 6e**). With the 4.8 N spring, the emitted volume and mRNA

content were widely dispersed, whereas the values obtained with the 8.0 and 11.2 N springs clustered closely around the line. Consistent with these findings, the emitted mRNA concentration, calculated as the mRNA content per unit volume, remained stable with the 8.0 and 11.2 N springs (0.53 and 0.56 ng/μL; coefficients of variation of 8.1% and 7.2%, respectively). By comparison, the concentration obtained with the 4.8 N spring was higher and substantially more variable (0.69 ng/μL; coefficient of variation, 30.0%). These findings indicate that, once a stable spray was established at the higher compression forces, the device delivered a consistent mRNA concentration irrespective of the precise emitted volume. In contrast, the unstable spray generated with the 4.8 N spring compromised the uniformity of both the emitted volume and mRNA content.



371

372 **Fig. 6** Single-actuation mRNA content and volume as a function of spring compression force (4.8, 8.0, and 11.2
373 N) and actuation conditions. **a** mRNA content and **b** volume according to actuation speed (80, 130, and 180 mm/s)
374 at a fixed actuation acceleration of 4,000 mm/s². **c** mRNA content and **d** volume according to actuation
375 acceleration (4,000, 8,000, and 12,000 mm/s²) at a fixed actuation speed of 180 mm/s. **e** Single-actuation mRNA

content plotted against emitted volume across all conditions, with symbol colors indicating spring compression force. Solid lines and shaded bands represent the linear regression and 95% confidence interval, respectively, for each compression force; the dashed line represents the theoretical relationship at a constant concentration. In **a–d**, data are presented as the mean ± SD (n = 3); *p < 0.05, **p < 0.01, ***p < 0.001, and ****p < 0.0001 versus 4.8 N; ####p < 0.0001 versus 8.0 N

Regional deposition in the nasal cast

Regional deposition was evaluated with particular emphasis on the middle and superior turbinates. Together, these regions received most of the dose deposited in the turbinates and were the most responsive to changes in the actuation conditions. Deposition in the nasal vestibule, inferior turbinate, and nasopharynx is presented in **Figs. 7a and 8a**. Before the actuation parameters were varied, the spray insertion angle was optimized by evaluating five angles ranging from 30° outward to 30° inward. The 30° outward angle resulted in the highest deposition in the superior turbinate and was therefore used in all subsequent deposition experiments (**Online Resource 1**). Notably, spring compression force and actuation speed redistributed the dose between the middle and superior turbinates in opposite directions.

Increasing the spring compression force at an actuation speed of 80 mm/s shifted deposition from the middle turbinate toward the superior turbinate (**Fig. 7**). At the lowest compression force of 4.8 N, deposition was concentrated in the middle turbinate (33.6 ± 7.4%), with only a small proportion reaching the superior turbinate (9.0 ± 3.5%). Increasing the compression force to 8.0 and 11.2 N reversed this distribution and significantly increased superior-turbinate deposition to 42.9 ± 3.5% and 38.9 ± 9.5%, respectively ($p < 0.01$; **Fig. 7c**). Correspondingly, middle-turbinate deposition decreased to 22.8 ± 5.1% and 24.7 ± 3.8%, respectively, although these differences were not significant (**Fig. 7b**).

Increasing the actuation speed with the 11.2 N spring produced the opposite redistribution, shifting deposition from the superior turbinate back toward the middle turbinate (**Fig. 8**). Superior-turbinate deposition remained high at 80 and 130 mm/s (38.9 ± 9.5% and 38.6 ± 7.1%, respectively), but decreased significantly to 11.5 ± 0.6% at 180 mm/s ($p < 0.01$; **Fig. 8c**). Concurrently, middle-turbinate deposition increased significantly from 24.7 ± 3.8% at 80 mm/s and 23.2 ± 5.5% at 130 mm/s to 43.5 ± 2.7% at 180 mm/s (**Fig. 8b**).

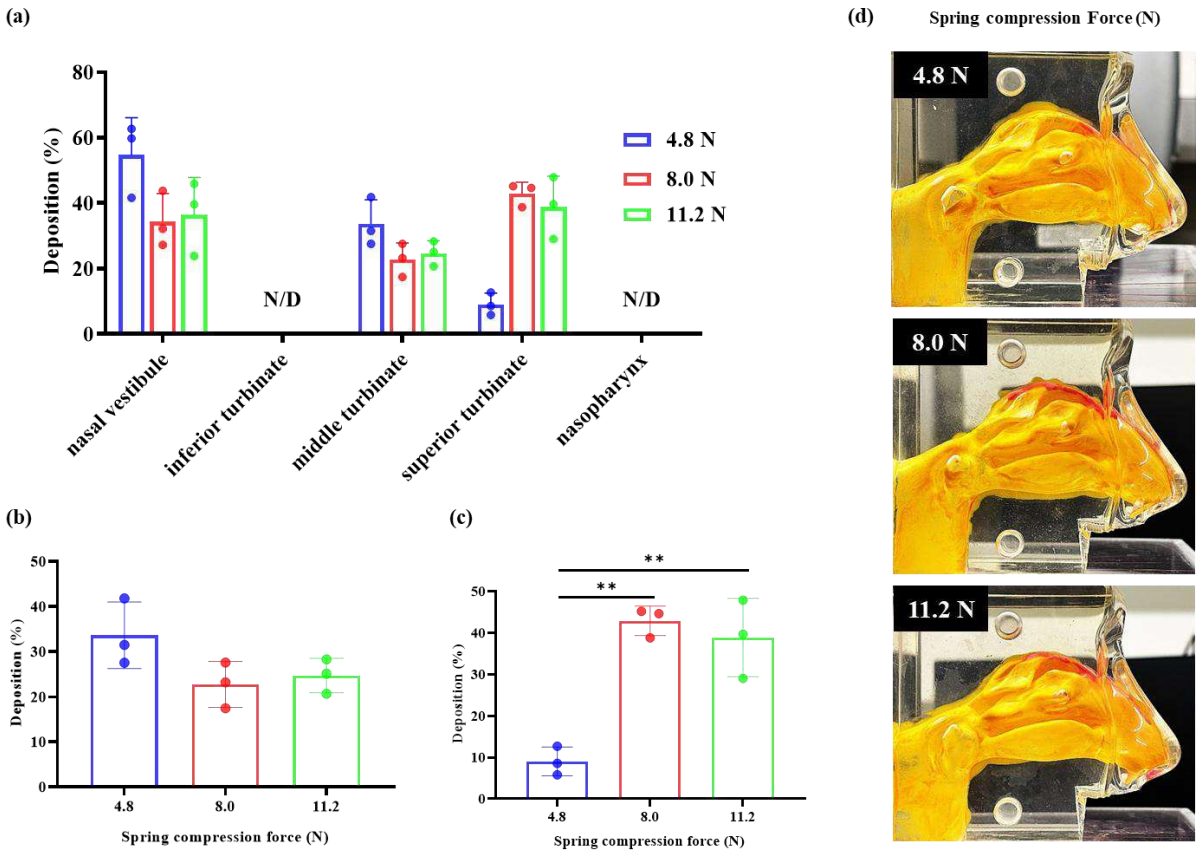
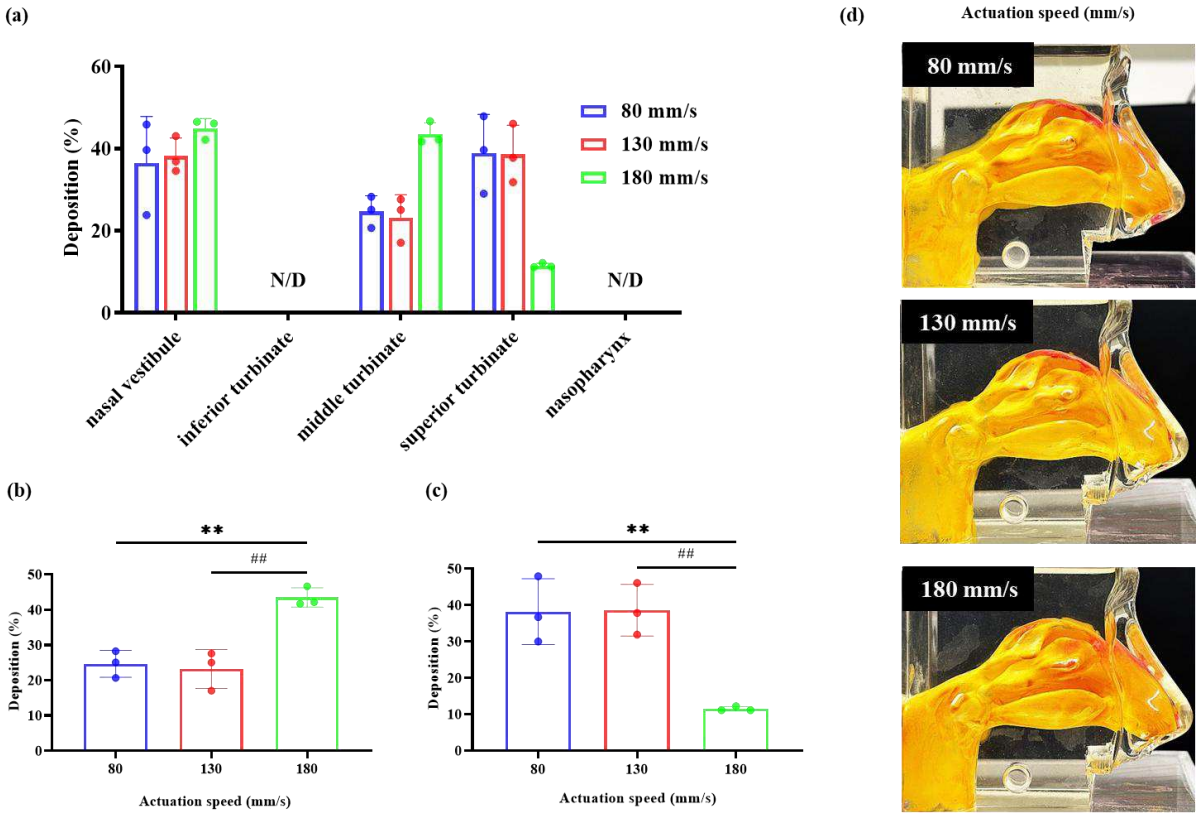


Fig. 7 Regional deposition in the nasal cast as a function of spring compression force (4.8, 8.0, and 11.2 N) at a fixed actuation speed of 80 mm/s and an outward spray angle of 30°. **a** Deposition (%) in each region (nasal vestibule, inferior turbinate, middle turbinate, superior turbinate, and nasopharynx); N/D, not detected. **b** Middle-turbinate deposition. **c** Superior-turbinate deposition. **d** Representative images of the nasal cast at each spring compression force, with deposited regions visualized by changes in the color of the water-finding paste. Data are presented as the mean ± SD (n = 3); **p < 0.01 versus 4.8 N.



412

413 **Fig. 8** Regional deposition in the nasal cast as a function of actuation speed (80, 130, and 180 mm/s) with the 11.2
414 N spring at an outward spray angle of 30°. **a** Deposition (%) in each region; N/D, not detected. **b** Middle-turbinate
415 deposition. **c** Superior-turbinate deposition. d Representative images of the nasal cast at each actuation speed.
416 Data are presented as the mean ± SD (n = 3); **p < 0.01 versus 80 mm/s; ##p < 0.01 versus 130 mm/s.

417

418 **Effect of actuation on mRNA-LNP integrity**

419 Actuation compromised the physicochemical integrity of the mRNA-LNPs, and the extent of this effect varied
420 with spring compression force (**Fig. 9**). Before actuation, the LNPs were uniform, with a hydrodynamic diameter
421 of 90.2 ± 0.2 nm, a low polydispersity index, and an EE of 86.1 ± 0.5% (**Fig. 9a–c**). Following actuation, the
422 hydrodynamic diameter increased markedly, with the magnitude of the increase rising with compression force.
423 The mean diameter increased to 163 ± 20 nm at 4.8 N, 379 ± 574 nm at 8.0 N, and 1,063 ± 783 nm at 11.2 N. The
424 higher compression forces therefore produced large, micron-sized aggregates that exceeded the 200 nm threshold
425 and varied substantially among replicates (**Fig. 9a**). EE decreased significantly at every compression force, from
426 86.1% before actuation to 40.8 ± 9.9%, 48.1 ± 7.7%, and 54.8 ± 4.0% at 4.8, 8.0, and 11.2 N, respectively (**Fig.**

9c). In contrast, the polydispersity index and zeta potential remained largely unchanged and showed no consistent relationship with compression force (**Fig. 9b, d**).

Although the increase in particle size was smallest at the lowest compression force of 4.8 N, EE under this condition was reduced by approximately half. This finding indicates that the relative preservation of particle size did not reflect preservation of the encapsulated cargo. Across all compression forces, the EE decreased to 40–55% of the pre-actuation value, showing that adjusting the device actuation conditions alone was insufficient to preserve mRNA-LNP integrity during spray delivery in the absence of stabilizing excipients.

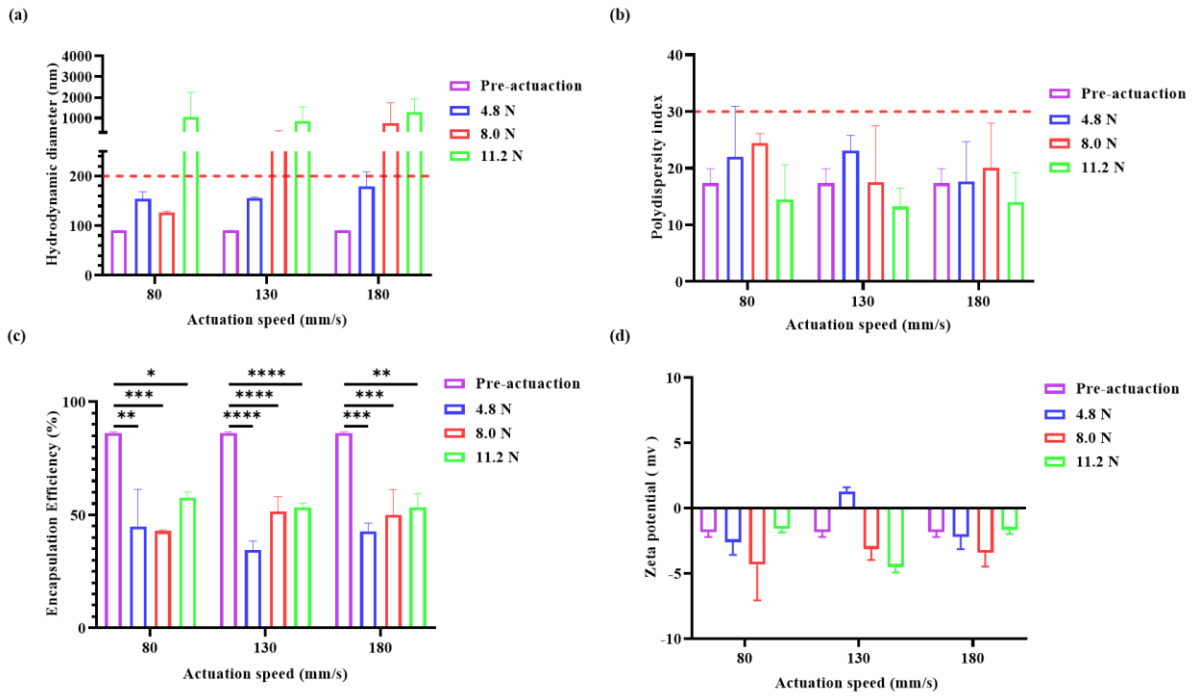


Fig. 9 Physicochemical properties of mRNA-loaded LNPs before and after actuation at spring compression forces of 4.8, 8.0, and 11.2 N and actuation speeds of 80, 130, and 180 mm/s. **a** Hydrodynamic diameter, **b** polydispersity index, **c** encapsulation efficiency, and **d** zeta potential, with the pre-actuation values shown for reference. The red dashed lines indicate thresholds of 200 nm in a and 30 in b. Data are presented as the mean ± SD (n = 3); *p < 0.05, **p < 0.01, ***p < 0.001, and ****p < 0.0001

Excipient screening for LNP stabilization

To determine whether stabilizing excipients could preserve mRNA-LNP integrity during actuation, LNPs were formulated with hyaluronic acid (HA), poly(vinyl alcohol) 2000 (PVA 2000), or hydroxypropyl methylcellulose (HPMC) and evaluated before and after actuation at 11.2 N and 80 mm/s (**Fig. 10**). In the absence of an excipient, the LNPs underwent severe aggregation following actuation: the hydrodynamic diameter increased from 90.2 ± 0.2 nm to 1,052 ± 1,189 nm, while the EE decreased from 86.1 ± 0.5% to 57.6 ± 2.5% (**Fig. 10a, c**). All three excipients suppressed aggregation and maintained the post-actuation hydrodynamic diameter below 200 nm, with values of 129.7 ± 3.7 nm for HA, 116.6 ± 1.8 nm for HPMC, and 107.1 ± 0.9 nm for PVA 2000 (**Fig. 10a**).

The excipients differed, however, in their ability to preserve the encapsulated cargo. HA and PVA 2000 partially preserved EE, with post-actuation values of 68.9 ± 2.1% and 66.3 ± 1.2%, respectively. HPMC provided the greatest protection, with EE remaining essentially unchanged after actuation (84.7 ± 4.1% before actuation versus 84.9 ± 9.1% after actuation; **Fig. 10c**). The polydispersity index and zeta potential remained largely unchanged across all formulations (**Fig. 10b, d**).

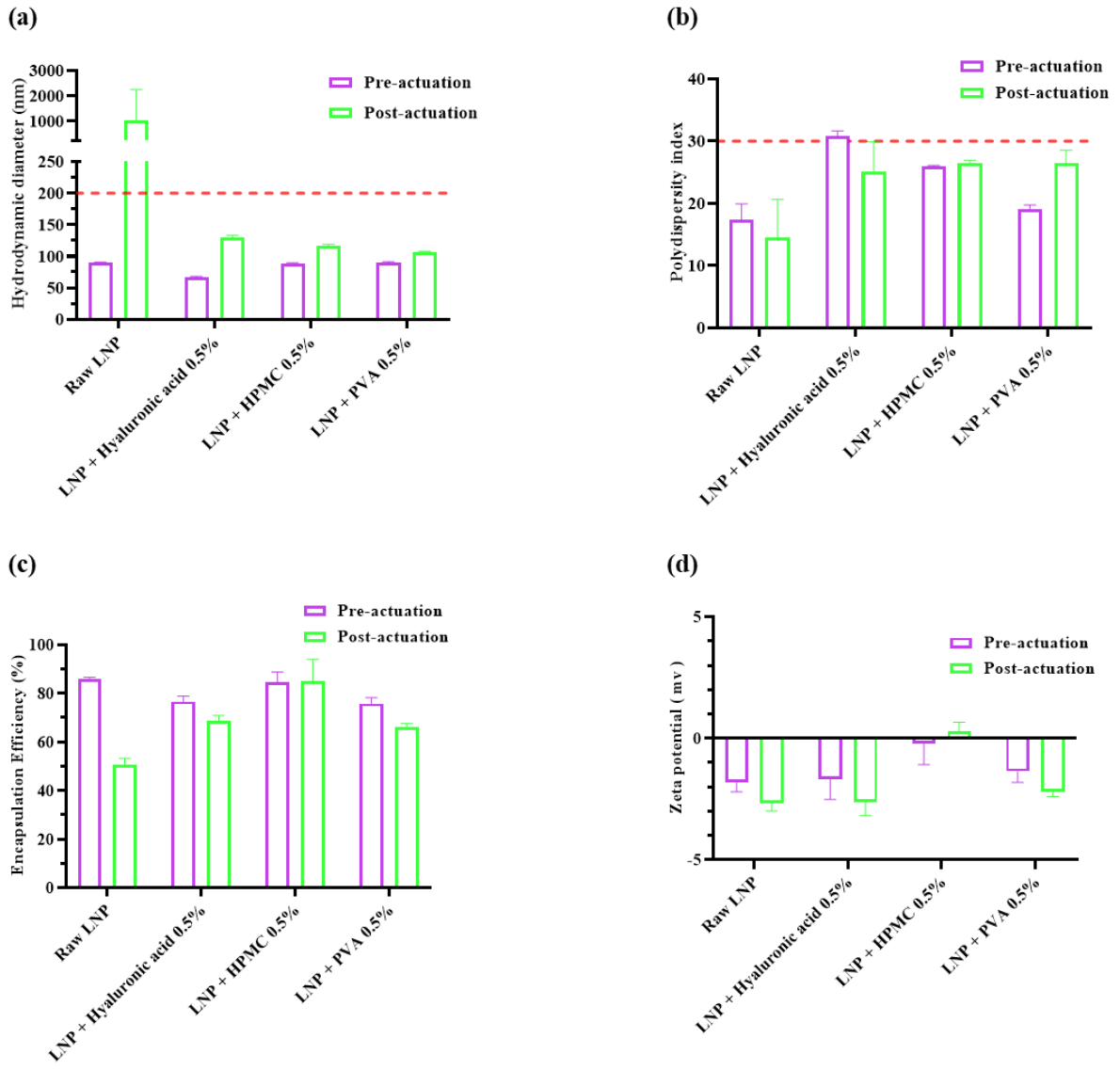


Fig. 10 Effects of stabilizing excipients on the physicochemical properties of mRNA-loaded LNPs before and after actuation. Raw LNPs and LNPs formulated with hyaluronic acid, HPMC, or PVA 2000 are compared. **a** Hydrodynamic diameter, **b** polydispersity index, **c** encapsulation efficiency, and **d** zeta potential, with the pre-actuation values shown for reference. The red dashed lines indicate 200 nm in **a** and 30 in **b**. Data are presented as mean ± SD (n = 3)

Plume geometry and spray pattern of the PVA-containing formulation

PVA was selected as the model excipient because, at the low concentration used here (0.5%), it provides LNP stabilization without the marked increase in solution viscosity associated with other candidate excipients All

spray-characterization experiments comparing PVA 0% and the PVA-containing formulation were conducted using the 11.2 N spring at an actuation speed of 80 mm/s. The addition of 0.5% PVA had minimal effect on the plume geometry or spray pattern relative to PVA 0% (**Fig. 11**). The plume angle was similar between the two solutions (45.98 ± 4.06° for PVA 0% and 54.77 ± 3.74° for 0.5% PVA; **Fig. 11b**), as was the plume height, which remained within a narrow range (6.79 ± 0.64 and 9.77 ± 2.61 cm, respectively; **Fig. 11c**). The projected spray area was likewise comparable at both measurement distances. At 3 cm, the spray areas were 15.85 ± 0.55 cm^2 for PVA 0% and 17.68 ± 1.33 cm^2 for 0.5% PVA (**Fig. 11d**); at 6 cm, they were 44.63 ± 3.15 and 39.51 ± 0.54 cm^2, respectively (**Fig. 11e)**. The larger spray areas observed at 6 cm reflected continued radial expansion of the plume with distance. None of the plume-geometry or spray-pattern parameters differed significantly between PVA 0% and 0.5% PVA, indicating that the excipient did not significantly alter the macroscopic spray behavior. Representative images of the plume and spray patterns at 3 and 6 cm are shown in **Fig. 11a**.

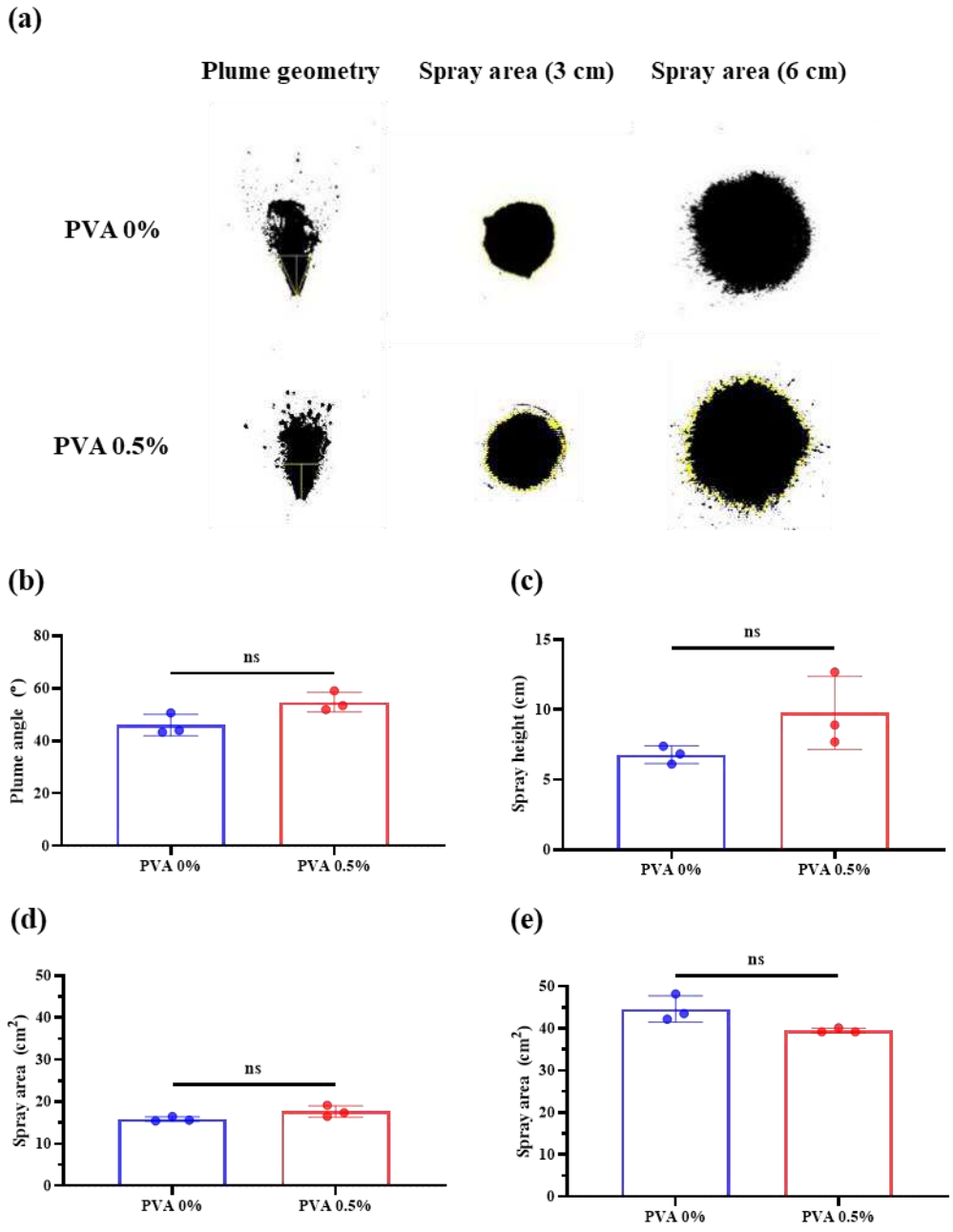


Fig. 11 Plume geometry and spray-pattern characteristics of 0% PVA and 0.5% PVA solutions. **a** Representative images of the plume geometry and spray patterns at 3 and 6 cm from the actuator orifice. **b** Plume angle, **c** plume height, **d** spray area at 3 cm, and **e** spray area at 6 cm. Data are presented as the mean ± SD (n = 3); groups were compared using an unpaired two-tailed t-test (ns, not significant)

Droplet size and spray transmission of the PVA-containing formulation

In contrast to its limited effect on plume geometry, the addition of 0.5% PVA markedly increased the atomized droplet size (**Fig. 12**). At 3 cm, the volume median diameter (Dv50) increased from 35.34 ± 0.10 µm for PVA 0% to 66.39 ± 0.78 µm for 0.5% PVA, while the Sauter mean diameter D[3,2] increased from 25.72 ± 0.07 to 49.02 ± 4.76 µm ($p < 0.0001$ and $p < 0.01$, respectively; **Fig. 12a**). A similar pattern was observed at 6 cm, where the Dv50 increased from 39.59 ± 0.23 to 61.60 ± 0.65 µm and the D[3,2] increased from 30.79 ± 0.36 to 51.13 ± 2.10 µm (both $p < 0.0001$; **Fig. 12b**). The proportion of the measurement period during which light transmission was below 90% was slightly higher for 0.5% PVA than for PVA 0% at 3 cm (26.72 ± 0.14% versus 26.10 ± 0.25%; $P < 0.05$) but did not differ significantly at 6 cm (29.96 ± 1.48% versus 27.36 ± 1.58%; ns).

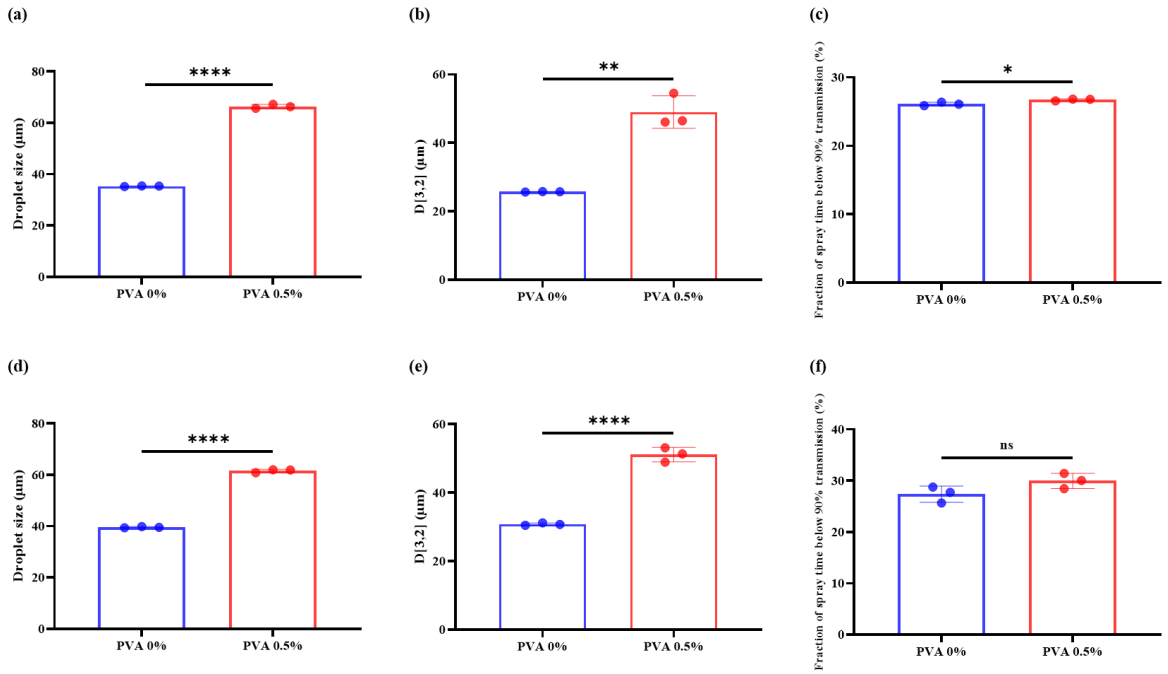


Fig. 12 Effect of PVA concentration on droplet size and spray duration. (a) Dv50, (b) D[3,2], and (c) fraction of spray time below 90% transmission at 3 cm; (d) Dv50, (e) D[3,2], and (f) fraction of spray time below 90% transmission at 6 cm. Data are presented as mean ± SD (n = 3). *$p < 0.05$, **$p < 0.01$, ****$p < 0.0001$; ns, not significant.

Regional nasal deposition of the PVA-containing formulation

Regional deposition was quantified in five regions of the nasal cavity cast: the nasal vestibule, inferior turbinate, middle turbinate, superior turbinate, and nasopharynx (**Fig. 13a**). For both solutions, deposition was concentrated

in the nasal vestibule and the middle and superior turbinates. The inferior turbinate received negligible proportions of the delivered dose (0.00 ± 0.00% for PVA 0% and 0.70 ± 1.22% for 0.5% PVA), and no deposition was detected in the nasopharynx (N/D). The addition of 0.5% PVA significantly increased deposition in the middle turbinate from 24.69 ± 3.83% for PVA 0% to 37.71 ± 2.86% for 0.5% PVA ($p < 0.01$; **Fig. 13b**). In contrast, superior-turbinate deposition did not differ significantly between PVA 0% and 0.5% PVA (38.86 ± 9.45% versus 32.73 ± 2.86%; ns; **Fig. 13c**). Deposition in the nasal vestibule was 36.46 ± 11.37% for PVA 0% and 28.86 ± 4.95% for 0.5% PVA (**Fig. 13a**). Representative images of the nasal cavity cast following administration of each solution are shown in **Fig. 13d**.

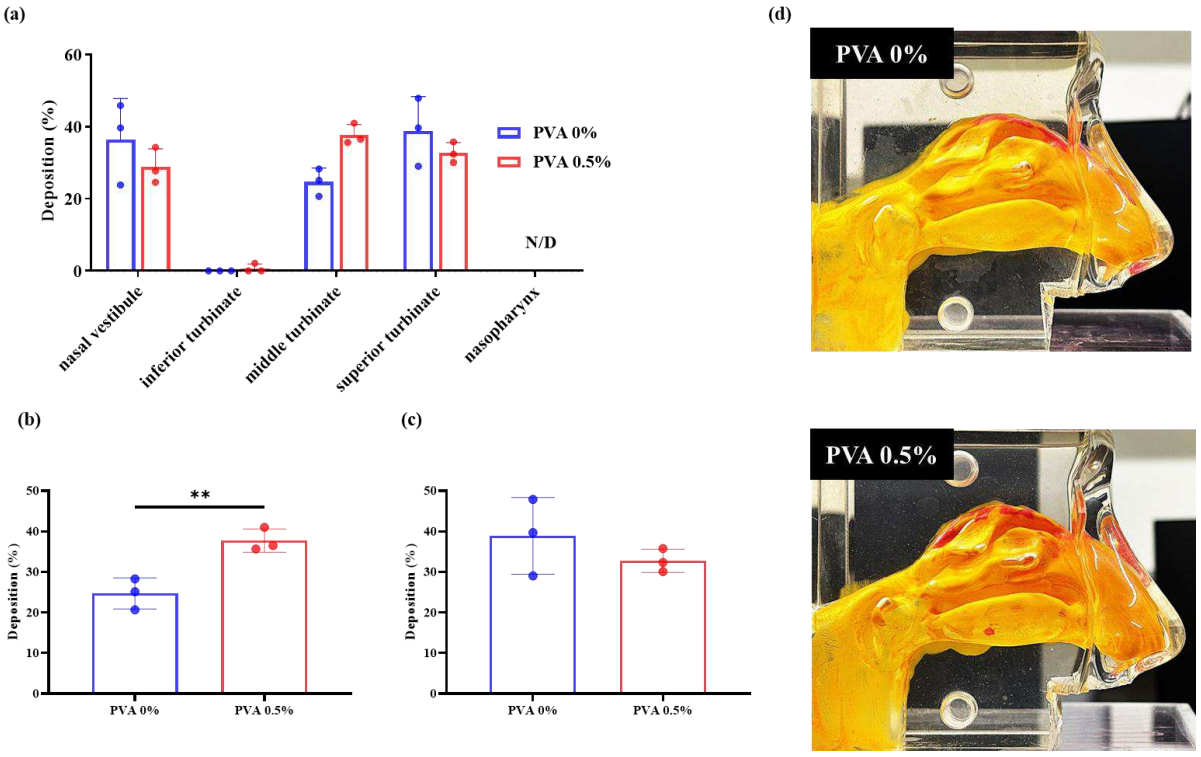


Fig. 13 Regional nasal deposition of PVA 0% and 0.5% PVA solutions in a nasal cavity cast. a Deposition (%) in the nasal vestibule, inferior turbinate, middle turbinate, superior turbinate, and nasopharynx (N/D, not detected). b Middle-turbinate and c superior-turbinate deposition for the two solutions. d Representative images of the nasal cavity cast after administration of PVA 0% (top) and 0.5% PVA (bottom). Data are presented as the mean ± SD (n = 3); groups were compared using an unpaired two-tailed t-test (**$p < 0.01$; ns, not significant)

Discussion

Our spray-characterization findings raise an important mechanistic question: why was the plume angle primarily associated with actuation speed, whereas droplet size was primarily associated with spring compression force? This apparent distinction can be understood by considering the sequence of events within a spring-driven, swirl-type pump, in which atomization occurs through two sequential stages governed by different inputs [42]. During the first stage, the liquid is forced through tangential passages into a swirl chamber, where it acquires angular momentum. The resulting centrifugal motion drives the liquid outward and creates a central air core, causing the formulation to emerge from the orifice as a thin, hollow conical sheet rather than a solid jet [42, 43]. The half-angle of this cone is determined by the balance between the tangential (swirling) and axial (forward) velocity components at the orifice. A greater tangential component widens the liquid sheet and opens the cone, whereas a greater axial component produces a narrower cone [42]. Increasing the actuation speed enhances the tangential velocity generated within the swirl chamber, which may explain the observed widening of the plume angle with increasing speed. This response reflects spray kinematics rather than the energy available for atomization [43].

During the second stage, the conical liquid sheet becomes progressively thinner as it expands. Aerodynamic instabilities then develop along its surface, fragmenting the sheet into ligaments that subsequently break into droplets [43]. Droplet size is governed by the energy available for this fragmentation, which scales with the atomization pressure. Because the spring compression force determines the pressure at which the liquid sheet is discharged, the stiffer springs generated finer droplets [21, 22, 42]. The plume angle and droplet size therefore represent distinct, complementary stages of the same atomization process: sheet formation, which is influenced by the swirl kinematics associated with actuation speed, and sheet breakup, which is driven by the pressure associated with spring compression force. The behavior of the weakest spring is consistent with this mechanism. At 4.8 N, the discharge pressure was apparently insufficient to generate a strong swirl or promote efficient sheet breakup. Consequently, the formulation left the orifice without forming a well-defined cone or fragmenting into fine droplets, resulting in the wide, unstable plume and coarse droplets observed experimentally. This two-stage mechanism thus provides a coherent explanation for the dependence of plume angle on actuation speed, the dependence of droplet size on compression force, and the failure of the weakest spring to produce a stable spray.

The effects of these two atomization stages extended beyond the device to influence regional dose deposition. Because sheet formation and sheet breakup responded to different actuation inputs, the plume entering the nasal

cavity had a geometry shaped predominantly by actuation speed and a droplet-size distribution shaped predominantly by compression force. Regional deposition responded differently to these characteristics. The finer, more forcefully propelled droplets generated at higher compression forces, reflecting more complete sheet breakup, carried a greater proportion of the dose upward and deeper into the superior turbinate, a region associated with olfactory transport to the brain [14, 19, 44]. Conversely, the wider cone produced at higher actuation speeds, reflecting stronger swirl during sheet formation, dispersed a greater proportion of the dose onto the middle turbinate before it could reach the superior region. Consequently, deposition in the middle and superior turbinates shifted in opposite directions as each actuation parameter increased.

These findings indicate that superior-turbinate targeting cannot be maximized simply by increasing the overall intensity of spray actuation. Increasing the compression force promoted the formation of finer droplets and enhanced superior-turbinate deposition. Increasing the actuation speed, however, widened the plume and redirected the dose toward the middle turbinate. The effects of the two atomization stages must therefore be balanced: compression force and actuation speed cannot be optimized independently because each influences a different spray characteristic that contributes to regional deposition. This interdependence represents the first level at which co-optimization of the device parameters is required.

The sheet breakup process that determines droplet size simultaneously exposes the suspended mRNA-LNPs to potentially damaging physical stresses. Although the mRNA-LNPs remained colloidally stable during storage at 4 °C, retaining their particle size and encapsulation efficiency during the first week, a single actuation was sufficient to compromise their integrity. Fragmentation of a thin liquid sheet into ligaments and droplets generates intense, transient shear and continuously creates new air–liquid interfaces. These conditions may disrupt the lipid nanoparticles and promote the release of their encapsulated cargo. Consistent with this mechanism, actuation reduced EE from 86.1% before actuation to 40.8–54.8% across the tested compression forces [20, 21]. The divergence between particle size and EE was particularly informative. At the lowest compression force, the hydrodynamic diameter was relatively well preserved, although EE had already decreased by approximately half. At higher compression forces, marked aggregation became evident, with particle sizes approaching or exceeding the approximately 200 nm threshold regarded as an upper limit for efficient nose-to-brain transport [15, 45]. Thus, the actuation conditions that promoted superior-turbinate deposition simultaneously threatened to shift the carriers beyond the size range considered favorable for this delivery route. Particle size, which is commonly used to

575 determine whether sprayed nanoparticles have retained their integrity, primarily reflects changes in the external
576 lipid structure. EE provides complementary information about retention of the payload and may therefore be a
577 more sensitive indicator of the functional dose remaining after actuation. The loss of encapsulated mRNA even
578 under the least forceful condition suggests that this damage was not confined to a single harsh actuation setting.
579 Because shear and interfacial stresses are intrinsic to sheet breakup, modification of the device parameters alone
580 was insufficient to preserve the encapsulated cargo.

581 This interpretation provided the rationale for screening stabilizing excipients capable of mitigating the physical
582 stresses generated during atomization. All three excipients limited the actuation-induced increase in particle size,
583 although their ability to preserve the encapsulated mRNA differed, with HPMC providing the greatest protection.
584 This finding should be interpreted cautiously. The excipients that most effectively retained the cargo were those
585 that increased the viscosity of the formulation, suggesting that greater continuous-phase viscosity may attenuate
586 the transmission of shear and interfacial stresses to individual particles during sheet breakup. This explanation is
587 consistent with reports that viscous cellulose-ether networks can protect nanoparticles during atomization-based
588 processing [46]. Direct rheological and interfacial measurements would be required to confirm this mechanism
589 and were beyond the scope of the present study. Accordingly, the current findings support the more limited
590 conclusion that formulation modification can mitigate the actuation-induced loss of LNP integrity that could not
591 be prevented through adjustment of the device parameters alone.

592 In addition to mitigating this loss, the formulation altered the spray in a manner that could be interpreted within
593 the same two-stage atomization framework. When 0.5% PVA was used as a representative viscosity-modifying
594 excipient, plume geometry remained unchanged, whereas droplet size approximately doubled at both
595 measurement distances. The formulation therefore altered the outcome of sheet breakup without measurably
596 affecting sheet formation. This distinction is mechanistically informative. A dilute polymer solution may increase
597 bulk shear viscosity only marginally, and droplet size in Newtonian sprays is generally insensitive to shear
598 viscosity across a broad range because it is governed primarily by the balance between inertial and surface-tension
599 forces [47]. The magnitude of the observed increase in droplet size may therefore reflect the extensional and
600 elastic response of the dissolved polymer rather than bulk shear viscosity alone. Such a response could resist
601 ligament thinning during breakup and generate larger droplets, consistent with reports that the median droplet size
602 of dilute polymer sprays increases with the extensional relaxation time of the liquid [48].

Functionally, the coarser droplets produced by the PVA-containing formulation increased deposition in the middle turbinate, while superior-turbinate deposition remained unchanged. This result is broadly consistent with the relationship between droplet size and regional deposition observed when the device parameters were varied, although the effect in this case originated from the formulation rather than the device. The formulation therefore provides an additional means of modulating regional deposition by acting on the sheet breakup stage that is influenced by compression force.

Collectively, these findings place the two stages of atomization at the center of nasal mRNA-LNP delivery. Sheet formation contributes to plume geometry, while sheet breakup determines droplet size and exposes the LNPs to stresses that can compromise cargo retention. Compression force promoted superior-turbinate deposition by generating finer droplets, although the same atomization process impaired LNP integrity. Regional deposition and cargo preservation are therefore not independent objectives that can be optimized sequentially; rather, they are coupled outcomes of a single atomization event. The formulation acts within this same process. A viscosity-modifying excipient not only protected the LNPs to varying degrees but also increased droplet size and redistributed deposition between the turbinates. The formulation should therefore be regarded not merely as a passive means of protecting the cargo but as an active determinant of spray performance and regional deposition.

The practical implication is that the delivery device and formulation must be developed concurrently. Actuation conditions should be tuned to promote deposition in the superior turbinate, while the formulation should be designed to withstand the stresses imposed by sheet breakup. This process must account for the capacity of the formulation itself to modify droplet size and thereby alter regional deposition.

Several areas warrant further investigation. In the present study, spray characterization was designed to isolate the effects of the actuation parameters. A natural next step is therefore to characterize spray behavior using the complete LNP formulation, whose viscosity and surface activity may influence both sheet formation and sheet breakup. Such experiments would link the atomization behavior of the device more directly to the physicochemical properties of the formulation. In particular, the finding that a viscosity-modifying excipient increased droplet size without altering plume geometry warrants direct characterization of the sprayed solutions under both shear and extensional flow. These measurements could determine whether polymer elasticity underlies the observed response and may allow droplet size, and consequently regional deposition, to be predicted from measurable formulation properties.

A broader device-design space should also be examined. In addition to spring compression force and actuation kinematics, nozzle geometry, swirl-chamber geometry, precompression, and metered volume may influence atomization and deposition. Systematic evaluation of these parameters would help define the extent to which superior-turbinate deposition can be increased before loss of cargo integrity becomes limiting. Finally, the biological consequences of delivery under the optimized conditions—including cellular uptake, mRNA expression, and in vivo N2B transport—remain to be established. Within these limitations, the present results demonstrate a generalizable principle: the actuation conditions that direct a nasal spray toward the superior turbinate also influence the integrity of its mRNA-LNP cargo. An integrated device–formulation framework therefore provides a rational basis for engineering nasal sprays capable of delivering mRNA-LNPs to the intended region while preserving their functional integrity.

Conclusion

This study demonstrates that the delivery device and formulation cannot be developed independently for nasal administration of mRNA-LNPs. The actuation conditions of the mechanical nasal spray pump governed regional deposition and LNP integrity simultaneously. Increasing the spring compression force promoted deposition in the superior turbinate, a region relevant to N2B transport, while actuation reduced the EE of the LNPs. The decline in EE occurred even when changes in particle size were limited, indicating that EE was a more sensitive measure of actuation-induced loss of integrity than particle size alone.

Because regional deposition and cargo preservation responded to the same actuation process, optimization of the device parameters alone was insufficient to achieve both objectives. Excipient screening showed that formulation modification could mitigate the actuation-induced loss of LNP integrity. In addition, 0.5% PVA increased droplet size and altered regional deposition without significantly changing plume geometry, demonstrating that the formulation, like the device, actively influences where the administered dose is deposited.

Nasal mRNA-LNP delivery should therefore be approached as an integrated device–formulation problem. Actuation parameters that promote superior-turbinate deposition must be paired with a formulation capable of withstanding the resulting atomization stresses, while accounting for the formulation's own effects on droplet size

and deposition. This framework provides a rational basis for developing nasal sprays that deliver intact, functional mRNA-LNPs to the intended nasal region. In vivo validation of nose-to-brain transport and mRNA expression will be essential to establish the biological relevance of these findings.

References

1. Bhunia S, Kolishetti N, Vashist A, Yndart Arias A, Brooks D, Nair M. Drug delivery to the brain: recent advances and unmet challenges. Pharmaceutics. 2023;15:2658. https://doi.org/10.3390/pharmaceutics15122658

2. Nguyen P-AT, Nguyen T-D, Park S. Advanced gene therapy in Parkinson's disease through innovations in drug delivery systems. J Pharm Investig. 2025;55:661–89. https://doi.org/10.1007/s40005-025-00739-5

3. de Koning LA, Vazquez-Matias DA, Beaino W, Vugts DJ, van Dongen GAMS, van der Flier WM, et al. Drug delivery strategies to cross the blood–brain barrier in Alzheimer's disease: a comprehensive review on three promising strategies. J Prev Alzheimers Dis. 2025;12:100204. https://doi.org/10.1016/j.tjpad.2025.100204

4. Wong KH, Riaz MK, Xie Y, Zhang X, Liu Q, Chen H, et al. Review of current strategies for delivering Alzheimer's disease drugs across the blood–brain barrier. Int J Mol Sci. 2019;20:381. https://doi.org/10.3390/ijms20020381

5. Liu J, Wang T, Dong J, Lu Y. The blood–brain barriers: novel nanocarriers for central nervous system diseases. J Nanobiotechnology. 2025;23:146. https://doi.org/10.1186/s12951-025-03247-8

6. Saraswathi TS, Mothilal M, Bukke SPN, Thalluri C, Chettupalli AK. Recent advances in potential drug nanocarriers for cns disorders: a review. Biomed Eng OnLine. 2025;24:137. https://doi.org/10.1186/s12938-025-01474-6

7. Saxena S, Mandrah V, Tariq W, Das P, Sambhav K, Devi SH. The future of mRNA vaccines: potential beyond COVID-19. Cureus. 2025;17:e84529. https://doi.org/10.7759/cureus.84529

8. Lu X, Fan S, Cao M, Liu D, Xuan K, Liu A. Extracellular vesicles as drug delivery systems in therapeutics: current strategies and future challenges. J Pharm Investig. 2024;54:785–802. https://doi.org/10.1007/s40005-024-00699-2

9. Hou X, Zaks T, Langer R, Dong Y. Lipid nanoparticles for mRNA delivery. Nat Rev Mater. 2021;6:1078–94. https://doi.org/10.1038/s41578-021-00358-0

686 10. Schober GB, Story S, Arya DP. A careful look at lipid nanoparticle characterization: analysis of benchmark
687 formulations for encapsulation of RNA cargo size gradient. Sci Rep. 2024;14:2403.
688 https://doi.org/10.1038/s41598-024-52685-1
689 11. Fan Y, Marioli M, Zhang K. Analytical characterization of liposomes and other lipid nanoparticles for drug
690 delivery. J Pharm Biomed Anal. 2021;192:113642. https://doi.org/10.1016/j.jpba.2020.113642
691 12. Kim H, Kim S, Lee D, Lee D, Yoon J, Lee H. Oligonucleotide therapeutics and their chemical modification
692 strategies for clinical applications. J Pharm Investig. 2024;54:415–33. https://doi.org/10.1007/s40005-024-00669-
693 8
694 13. Chung K, Ko H-G, Yi Y, Chung S-E, Lim J, Park S, et al. Intranasal delivery of siRNA targeting NR2B
695 attenuates cancer-associated neuropathic pain. J Pharm Investig. 2024;54:483–95.
696 https://doi.org/10.1007/s40005-024-00667-w
697 14. Nguyen TTL, Maeng HJ. Pharmacokinetics and pharmacodynamics of intranasal solid lipid nanoparticles and
698 nanostructured lipid carriers for nose-to-brain delivery. Pharmaceutics. 2022;14:572.
699 https://doi.org/10.3390/pharmaceutics14030572
700 15. Koo J, Lim C, Oh KT. Recent advances in intranasal administration for brain-targeting delivery: a
701 comprehensive review of lipid-based nanoparticles and stimuli-responsive gel formulations. Int J Nanomedicine.
702 2024;19:1767–807. https://doi.org/10.2147/IJN.S439181
703 16. Gandhi S, Shastri DH, Shah J, Nair AB, Jacob S. Nasal delivery to the brain: harnessing nanoparticles for
704 effective drug transport. Pharmaceutics. 2024;16:481. https://doi.org/10.3390/pharmaceutics16040481
705 17. Djupesland PG. Nasal drug delivery devices: characteristics and performance in a clinical perspective—a
706 review. Drug Deliv Transl Res. 2013;3:42–62. https://doi.org/10.1007/s13346-012-0108-9
707 18. Gänger S, Schindowski K. Tailoring formulations for intranasal nose-to-brain delivery: a review on
708 architecture, physico-chemical characteristics and mucociliary clearance of the nasal olfactory mucosa.
709 Pharmaceutics. 2018;10:116. https://doi.org/10.3390/pharmaceutics10030116
710 19. Tong X, Dong J, Shang Y, Inthavong K, Tu J. Effects of nasal drug delivery device and its orientation on
711 sprayed particle deposition in a realistic human nasal cavity. Comput Biol Med. 2016;77:40–8.
712 https://doi.org/10.1016/j.compbiomed.2016.08.002
713 20. Inthavong K, Tian ZF, Li HF, Tu JY, Yang W, Xue CL, et al. A numerical study of spray particle deposition in
714 a human nasal cavity. Aerosol Sci Technol. 2006;40:1034–45. https://doi.org/10.1080/02786820600924978
715 21. Guo C, Doub WH. The influence of actuation parameters on in vitro testing of nasal spray products. J Pharm

716 Sci. 2006;95:2029–40. https://doi.org/10.1002/jps.20678
717 22. Liu X, Doub WH, Guo C. Assessment of the influence factors on nasal spray droplet velocity using phase-
718 Doppler anemometry (PDA). AAPS PharmSciTech. 2011;12:337–43. https://doi.org/10.1208/s12249-011-9594-
719 1
720 23. Mehta T, Najafian S, Patel K, Lacombe J, Chaudhuri B. Optimization of carrier-based dry powder inhaler
721 performance: a review. Pharmaceutics. 2025;17:96. https://doi.org/10.3390/pharmaceutics17010096
722 24. Kolanjiyil AV, Walenga R, Babiskin A, Golshahi L, Hindle M, Longest W. Establishing quantitative
723 relationships between changes in nasal spray in vitro metrics and drug delivery to the posterior nasal region. Int J
724 Pharm. 2023;635:122718. https://doi.org/10.1016/j.ijpharm.2023.122718
725 25. Kim J, Jozic A, Lin Y, Eygeris Y, Bloom E, Tan X, et al. Engineering lipid nanoparticles for enhanced
726 intracellular delivery of mRNA through inhalation. ACS Nano. 2022;16:14792–806.
727 https://doi.org/10.1021/acsnano.2c05647
728 26. Lewis MM, Soto MR, Maier EY, Wulfe SD, Bakheet S, Obregon H, et al. Optimization of ionizable lipids for
729 aerosolizable mRNA lipid nanoparticles. Bioeng Transl Med. 2023;8:e10580. https://doi.org/10.1002/btm2.10580
730 27. Kim J, Jozić A, Bloom E, Jones B, Marra M, Murthy NTV, et al. Microfluidic platform enables shearless
731 aerosolization of lipid nanoparticles for mRNA inhalation. ACS Nano. 2024;18:11335–48.
732 https://doi.org/10.1021/acsnano.4c00768
733 28. Zhang H, Leal J, Soto MR, Smyth HDC, Ghosh D. Aerosolizable lipid nanoparticles for pulmonary delivery
734 of mRNA through design of experiments. Pharmaceutics. 2020;12:1042.
735 https://doi.org/10.3390/pharmaceutics12111042
736 29. Szabová J, Mišík O, Havlíková M, Lízal F, Mravec F. Influence of liposomes composition on their stability
737 during the nebulization process by vibrating mesh nebulizer. Colloids Surf B Biointerfaces. 2021;204:111793.
738 https://doi.org/10.1016/j.colsurfb.2021.111793
739 30. Kim B, Park B, You S, Jung SH, Lee S, Lim K, et al. Cell membrane camouflaged nanoparticle strategy and
740 its application in brain disease: a review. J Pharm Investig. 2024;54:435–51. https://doi.org/10.1007/s40005-024-
741 00680-z
742 31. Song B, Cho C-W. Applying polyvinyl alcohol to the preparation of various nanoparticles. J Pharm Investig.
743 2024;54:249–66. https://doi.org/10.1007/s40005-023-00649-4
744 32. Cortés H, Hernández-Parra H, Bernal-Chávez SA, Prado-Audelo MLD, Caballero-Florán IH, Borbolla-
745 Jiménez FV, et al. Non-ionic surfactants for stabilization of polymeric nanoparticles for biomedical uses. Materials

(Basel). 2021;14:3197. https://doi.org/10.3390/ma14123197

33. Park H, Lee J, Hwang J, Mohanto N, Lee HJ, Park J, et al. Stabilization of perfluorocarbon nanoemulsions using plasma volume expanders for artificial blood applications. J Pharm Investig. 2026; https://doi.org/10.1007/s40005-026-00806-5

34. Liu K, Huang X. Synthesis of self-assembled hyaluronan based nanoparticles and their applications in targeted imaging and therapy. Carbohydr Res. 2022;511:108500. https://doi.org/10.1016/j.carres.2022.108500

35. Wang G, Zhai Z, Wang W, Xia X, Guo H, Yue X, et al. Tailored borneol-modified lipid nanoparticles nasal spray for enhanced nose-to-brain delivery to central nervous system diseases. ACS Nano. 2024;18:23684–701. https://doi.org/10.1021/acsnano.4c08279

36. Guo H, Wang G, Zhai Z, Huang J, Huang Z, Zhou Y, et al. Rivastigmine nasal spray for the treatment of Alzheimer's disease: olfactory deposition and brain delivery. Int J Pharm. 2024;652:123809. https://doi.org/10.1016/j.ijpharm.2024.123809

37. US Food and Drug Administration. Bioavailability and bioequivalence studies for nasal aerosols and nasal sprays for local action. Rockville, MD: US Food and Drug Administration; 2003.

38. United States Pharmacopeial Convention General chapter <601> inhalation and nasal drug products: aerosols, sprays, and powders—performance quality tests. Rockville, MD: United States Pharmacopeial Convention; 2021.

39. Wang H, Zhang Y, Zhang Y, Kelleher A, Ahlenstiel C, Zhang MX, et al. Evaluation of Rayleigh jet atomizer for intranasal delivery of lipid nanoparticle-siRNA formulations: stability, deposition, and device performance. Int J Pharm. 2025;683:126084. https://doi.org/10.1016/j.ijpharm.2025.126084

40. Park H, Lee J, Kang J-W, Min J-Y, Lee J, Hong J, et al. Cationic lipid nanoparticles for nucleic acid delivery: microfluidics versus thin film hydration. J Pharm Investig. 2025;56:343–56. https://doi.org/10.1007/s40005-025-00737-7

41. Jang E, Lee Y, Ko E, Jeong M, Chang J, Lee H. Development of lipid nanoparticle formulation for intramuscular administration of mRNA vaccine against respiratory syncytial virus. J Pharm Investig. 2025;55:735–47. https://doi.org/10.1007/s40005-024-00719-1

42. Khani Aminjan K, Ghodrat M, Escobedo-Diaz JP, Heidari M, Chitt M, Hajivand M. Study on inlet pressure and Reynolds number in pressure-swirl atomizer with spiral path. Int Commun Heat Mass Transf. 2022;137:106231. https://doi.org/10.1016/j.icheatmasstransfer.2022.106231

43. Ding J-W, Li G-X, Yu Y-S, Li H-M. Numerical investigation on primary atomization mechanism of hollow cone swirling sprays. Int J Rotating Mach. 2016;2016:1–11. https://doi.org/10.1155/2016/1201497

44. Ko E, Hu J, Jeong Y, Oh C, Abdus SM, Lee BJ, et al. Advances in pharmaceutical formulation technologies for thermostable vaccine platforms considering patient-centered design. J Pharm Investig. 2025;56:903–39. https://doi.org/10.1007/s40005-025-00795-x

45. Boyuklieva R, Pilicheva B. Micro- and nanosized carriers for nose-to-brain drug delivery in neurodegenerative disorders. Biomedicines. 2022;10:1706. https://doi.org/10.3390/biomedicines10071706

46. Wan KY, Weng J, Wong SN, Kwok PCL, Chow SF, Chow AHL. Converting nanosuspension into inhalable and redispersible nanoparticles by combined in-situ thermal gelation and spray drying. Eur J Pharm Biopharm. 2020;149:238–47. https://doi.org/10.1016/j.ejpb.2020.02.010

47. Kooij S, Sijs R, Denn MM, Villermaux E, Bonn D. What determines the drop size in sprays? Phys Rev X. 2018;8:031019. https://doi.org/10.1103/PhysRevX.8.031019

48. Gaillard A, Sijs R, Bonn D. What determines the drop size in sprays of polymer solutions? J Non-Newtonian Fluid Mech. 2022;305:104813. https://doi.org/10.1016/j.jnnfm.2022.104813

Statements and Declarations

Authors' contributions

JSK: Conceptualization, Investigation, Formal analysis, Visualization, and Writing – Original draft preparation. **JHJ**: Investigation, Formal analysis, Visualization, Writing – Original draft preparation, and Writing – Review and editing. **YRC**: Investigation and Formal analysis. **WYJ**: Investigation and Formal analysis. **JHK**: Methodology and Resources. **YSS**: Methodology and Validation. **HJL**: Methodology and Supervision. **DHS**: Methodology, Resources, and Supervision. **CWP**: Conceptualization, Supervision, Funding acquisition, and Project administration. All authors have read and agreed to the published version of the manuscript.

Competing interests

The authors report no conflicts of interest

Funding

This work was supported by the National Research Foundation of Korea(NRF) grant funded by the Korea government(MSIT) (RS-2026-25479739, RS-2025-02273102), and this research was supported by a grant of the Korea Health Technology R&D Project through the Korea Health Industry Development Institute (KHIDI), funded by the Ministry of Health & Welfare, Republic of Korea (grant number : RS-2024-00335798). This work was supported by the Korea Environmental Industry & Technology Institute (KEITI) through the Technology Development Project for Safety Management of Household Chemical Products, funded by the Korea Ministry of Environment (MOE) (RS-2025-02223572). This work was partly supported by the Technology development Program of MSS (S3471143) and the Regional Innovation System & Education (RISE) program through the Chungbuk Regional Innovation System & Education Center, funded by the Ministry of Education (MOE) and the Chungcheongbuk-do, Republic of Korea (2026-RISE-11-014-03).

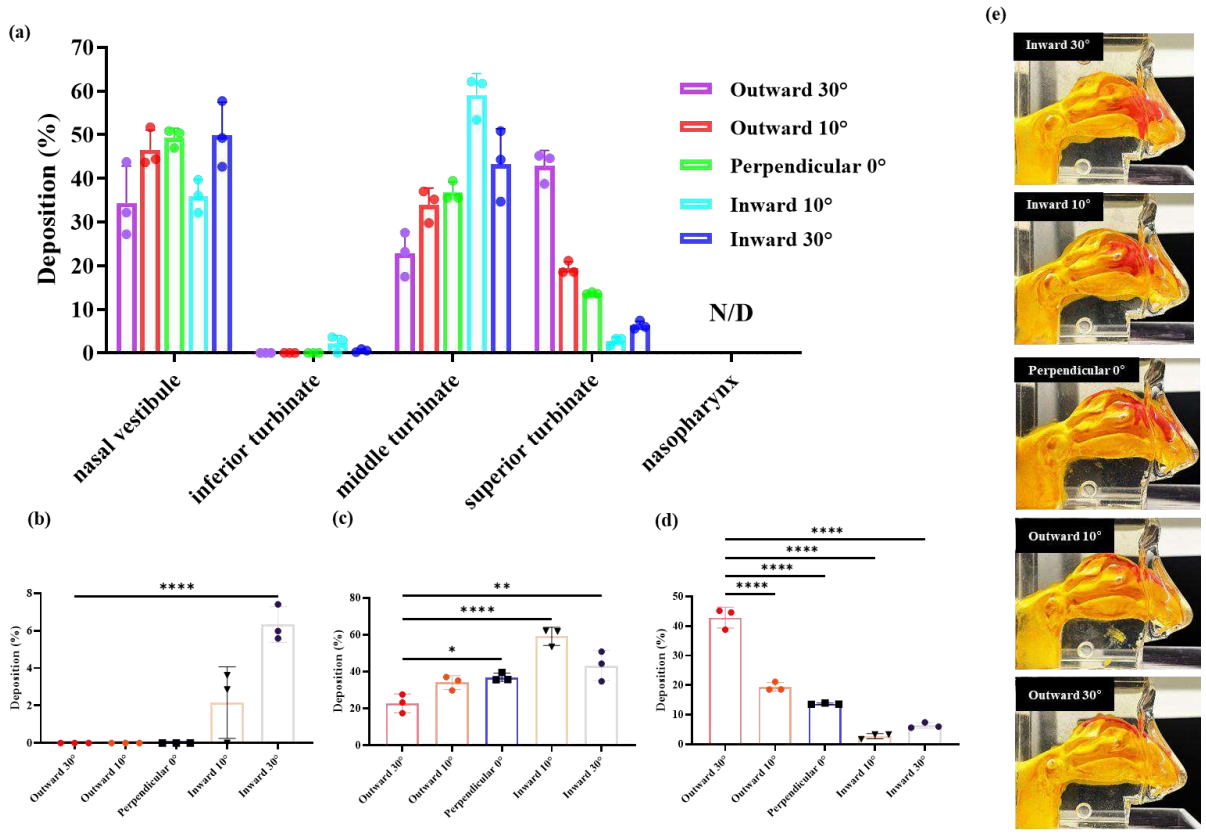
Data availability

The datasets generated and analyzed in this study are available from the corresponding author upon reasonable request.

Ethics approval

This study did not involve human participants or animals; ethics approval was not required

Supplementary Information



Online Resource 1. Effect of the spray insertion angle on regional deposition in the nasal cast, evaluated at five insertion angles (outward 30°, outward 10°, perpendicular 0°, inward 10°, and inward 30°) with the 11.2 N spring at 80 mm/s. **a** Deposition (%) in each region (nasal vestibule, inferior turbinate, middle turbinate, superior turbinate, and nasopharynx), with representative images of the nasal cast at each insertion angle shown on the right. **b** Inferior-turbinate, **c** middle-turbinate, and **d** superior-turbinate deposition as a function of the insertion angle. Data are presented as mean ± SD (n = 3); *p < 0.05, **p < 0.01, ****p < 0.0001 versus outward 30°.